

Inhibition of hypoxia-inducible factor 1 with acriflavine sensitizes hypoxic tumor cells to photodynamic therapy with zinc phthalocyanine-encapsulating cationic liposomes

Mans Broekgaarden¹, Ruud Weijer¹, Massis Krekorian¹, Bas van den IJssel¹, Milan Kos¹, Lindy K. Alles¹, Albert C. van Wijk¹, Zsolt Bikadi², Eszter Hazai², Thomas M. van Gulik¹, and Michal Heger¹ (✉)

¹ Department of Experimental Surgery, Academic Medical Center, University of Amsterdam, Meibergdreef 9, 1105 AZ Amsterdam, the Netherlands

² Virtua Drug Ltd., Csalogany 4C, H-1015, Budapest, Hungary

Received: 17 May 2015

Revised: 22 February 2016

Accepted: 28 February 2016

© Tsinghua University Press and Springer-Verlag Berlin Heidelberg 2016

KEYWORDS

cancer therapy,
confocal microscopy,
drug delivery system,
glucose metabolism,
hypoxia

ABSTRACT

Photodynamic therapy (PDT) is a tumor treatment modality in which a tumor-localized photosensitizer is excited with light, which results in local production of reactive oxygen species, destruction of tumor vasculature, tumor hypoxia, tumor cell death, and induction of an anti-tumor immune response. However, pre-existing tumor hypoxia may desensitize tumors to PDT by activating the hypoxia-inducible factor 1 (HIF-1) survival pathway. Therefore, we hypothesized that inhibition of HIF-1 with acriflavine (ACF) would exacerbate cell death in human epidermoid carcinoma (A431) cells. PDT of A431 tumor cells was performed using newly developed and optimized PEGylated cationic liposomes containing the photosensitizer zinc phthalocyanine (ZnPC). Molecular docking revealed that ACF binds to the dimerization domain of HIF-1 α , and confocal microscopy confirmed translocation of ACF from the cytosol to the nucleus under hypoxia. HIF-1 was stabilized in hypoxic, but not normoxic, A431 cells following PDT. Inhibition of HIF-1 with ACF increased the extent of PDT-induced cell death under hypoxic conditions and reduced the expression of the HIF-1 target genes *VEGF*, *PTGS2*, and *EDN1*. Moreover, co-encapsulation of ACF in the aqueous core of ZnPC-containing liposomes yielded an adjuvant effect on PDT efficacy that was comparable to non-encapsulated ACF. In conclusion, HIF-1 contributes to A431 tumor cell survival following PDT with liposomal ZnPC. Inhibition of HIF-1 with free or liposomal ACF improves PDT efficacy.

Address correspondence to m.heger@amc.uva.nl

1 Introduction

Photodynamic therapy (PDT) is a non-to-minimally invasive treatment modality approved for the treatment of various types of solid tumors. The therapy involves administration of a photosensitizer that accumulates in the tumor tissue and subsequent irradiation of the photosensitizer-replete tumor with laser light that excites the photosensitizer. The excited photosensitizer interacts with molecular oxygen (O_2) and produces singlet oxygen (1O_2) and/or superoxide ($O_2^{\cdot-}$) through type II and type I photochemical reactions, respectively [1]. These reactive oxygen species (ROS) induce oxidative damage that leads to the death of tumor cells and cells that comprise the tumor vasculature. These events culminate in vascular shutdown, hypoxia and hyponutrition in the tumor tissue, and an anti-tumor immune response [2]. PDT is successfully used in the treatment of a variety of tumors, although bladder cancers and nasopharyngeal carcinomas have been reported to respond relatively poorly to this treatment [3, 4].

An improvement in PDT efficacy may be achieved by selecting a photosensitizer with better physico-chemical properties in combination with improved tumor targeting. Metallated phthalocyanines, such as zinc phthalocyanine (ZnPC), possess several important advantages over currently approved photosensitizers. In particular, ZnPC absorbs light at a longer wavelength (674 nm) and has a substantially higher molar extinction coefficient ($2.74 \times 10^5 \text{ M}^{-1}\cdot\text{cm}^{-1}$) than conventional photosensitizers [5, 6]. However, ZnPC is highly hydrophobic ($\log P$ of ~ 8) and therefore must be employed in conjunction with a biologically compatible photosensitizer delivery system. ZnPC retains its photophysical and photochemical properties in liposomes [7, 8] and liposomal encapsulation enables the delivery of high amounts of ZnPC to tumor cells [6]. Another advantage of liposomes is that their lipid bilayer can be compositionally modified for a specific pharmacokinetic purpose, including targeting [9]. For these reasons, we have previously developed a neutrally charged ZnPC-containing liposomal formulation designed for passive targeting towards the tumor stroma [7] via the enhanced permeability and retention effect [10]. Although this modality was effective

in vitro, induction of damage to tumor stroma and perivascular tumor cells may not account for complete tumor eradication *in vivo*. Therefore, in addition to directing photosensitizers to tumor cells, targeting them to the tumor vascular endothelium poses an interesting alternative or supplementary treatment, which can be achieved with cationic liposomes [11–13]. The development and application of such liposomes for PDT may result in more effective shutdown of the tumor vasculature, more severe tumor hypoxia, and, as a result, improved therapeutic outcome [6].

However, the ability of tumor cells to survive hypoxic conditions due to the stimulating effect of preexisting tumor hypoxia may reduce tumoricidal efficacy of PDT [14]. Preexisting tumor hypoxia and constitutive activation of the hypoxia-inducible factor 1 transcription factor (HIF-1) occur when the tumor growth rate exceeds the rate of neoangiogenesis (Fig. 1) [15, 16]. Moreover, HIF-1 activation has been associated with resistance to chemo- and radiotherapy [17, 18]. With respect to PDT, HIF-1 activity was found to be increased following irradiation in a variety of *in vitro* and *in vivo* models [19–23]. Additionally, HIF-1 has been associated with resistance to PDT *in vitro* [24] and in esophageal cancer patients [25]. Inhibition of HIF-1 activity and downstream survival signaling may therefore improve therapeutic efficacy of PDT.

Since hypoxia is a preexisting condition in most tumors and because induction of HIF-1 by hypoxia triggers a plethora of survival mechanisms, HIF-1 has been targeted for pharmacological intervention in cancer therapy [26]. The mechanism of HIF-1 activation under normal physiological conditions and during PDT is summarized in Fig. 1. Under normoxic conditions, HIF-1 α is constantly degraded via O_2 -dependent hydroxylation of the Pro402 and Pro564 residues by prolyl-hydroxylases (PHDs) and/or of the Asn803 residue by the factor inhibiting HIF (FIH) [27]. Hydroxylated HIF-1 α binds to the Von Hippel-Lindau tumor suppressor protein (VHL) that promotes complexation with the E3 ubiquitin ligase (E3UL) and subsequent polyubiquitination (Ub) and proteasomal degradation [28, 29]. Hypoxia diminishes the extent of HIF-1 α hydroxylation by PHDs and FIH and leads to its stabilization and nuclear translocation [30]. An alternative route to HIF-1 activation is through ROS

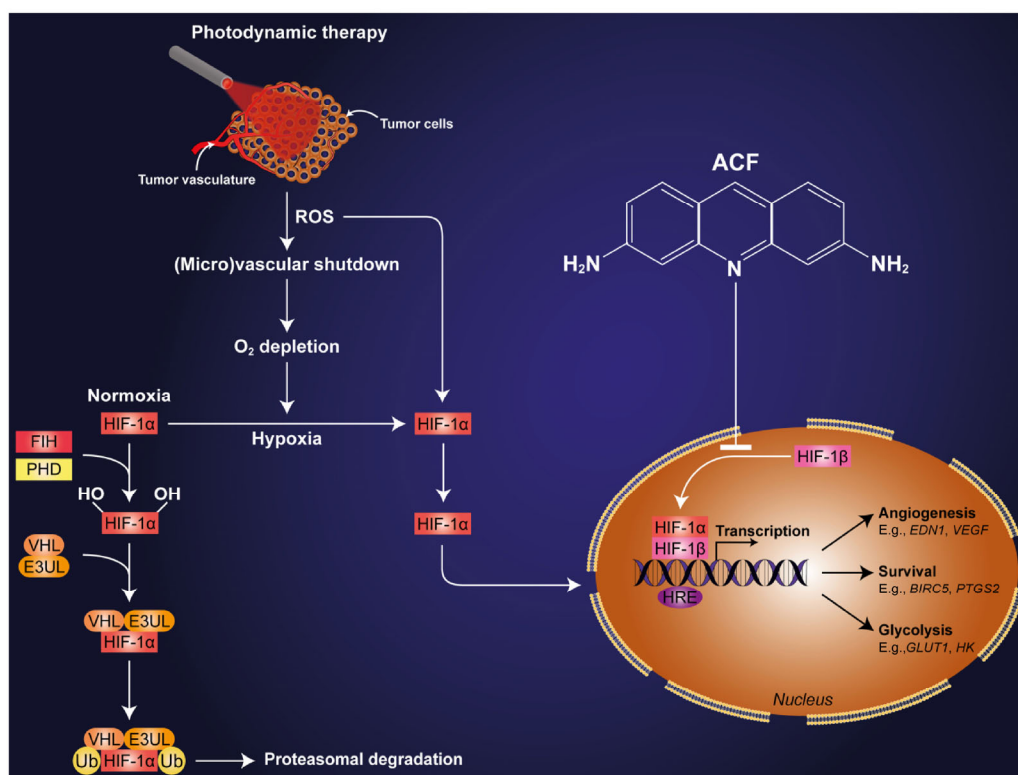


Figure 1 The HIF-1 signaling pathway in normoxia and hypoxia and the pharmacodynamics of ACF. Under normoxic conditions, HIF-1 α is constantly hydroxylated by PHDs and FIH, leading to VHL- and E3UL-dependent ubiquitination (Ub) and proteasomal degradation. After PDT, vascular shutdown causes tumor tissue hypoxia that abrogates HIF-1 α hydroxylation by PHD and FIH. Consequently, HIF-1 α translocates to the nucleus and dimerizes with HIF-1 β . The active HIF-1 dimer binds DNA at hypoxia-responsive elements and induces transcription of genes required for angiogenesis, survival, and glycolysis. ACF, which is readily taken up by tumor cells *in vivo* [81], blocks HIF-1 α /HIF-1 β dimerization by binding to HIF-1 α at its PAS dimerization domain, thereby reducing tumorigenicity of cancer cells [36].

that inhibit enzymatic activity of PHDs and FIH via oxidation of the redox-sensitive Fe(II) in the catalytic center [31, 32]. Following translocation to the nucleus, HIF-1 α dimerizes with HIF-1 β to bind DNA at the hypoxia-responsive elements in the promoter regions of many genes [33] that encode proteins involved in glycolysis, angiogenesis, survival, and apoptosis [15–17, 34, 35]. Inhibition of HIF-1 in PDT-treated tumor cells may therefore increase therapeutic efficacy.

In light of the prominent role of HIF-1 in the survival of tumor cells in hypoxic environments, this study aimed to determine whether inhibition of HIF-1 with acriflavine (ACF) during PDT with liposomal ZnPC can improve PDT outcome *in vitro*. ACF is a specific inhibitor of HIF-1 that prevents HIF-1 α /HIF-1 β dimerization by binding to the dimerization domain of HIF-1 α [36]. For these purposes, ZnPC-encapsulating cationic liposomes were developed that can be

specifically targeted to both the tumor vasculature [11, 12] and the tumor cells (this study). Thus, this formulation should concomitantly induce vascular shutdown, tumor hypoxia, and tumor cell death. The ultimate goal of this study was to design a PDT platform that would comprise a so-called fourth-generation photosensitizer (i.e., a second-generation photosensitizer (e.g., ZnPC) encapsulated in a photosensitizer delivery system (e.g., liposomes) with co-encapsulated inhibitors of survival pathways (e.g., ACF)). This photosensitizer delivery system will serve three main purposes, namely: (1) to damage the tumor endothelium and induce vascular shutdown and tumor hypoxia, (2) to kill tumor cells, and (3) to inhibit tumor cell survival pathways to prevent post-treatment tumor recovery. Accordingly, the cytotoxic effects of ACF in combination with PDT with ZnPC-encapsulating cationic liposomes were assessed in human epidermal

squamous cell carcinoma (A431) cells that represent a tumor type amenable for clinical treatment with PDT. Moreover, *in vitro* proof-of-concept studies with ZnPC + ACF-encapsulating cationic liposomes (i.e., the envisaged fourth-generation photosensitizer) were conducted in A431 cells. We showed that the ZnPC-liposomes are taken up by both endothelial and tumor cells, which leads to their enhanced susceptibility to PDT. Moreover, we demonstrated that both non-encapsulated and liposome-co-encapsulated ACF exerts an adjuvant effect on ZnPC-PDT efficacy in hypoxic tumor cells by reducing the expression of HIF-1 target genes. These results collectively validate the preclinical utility of this fourth-generation photosensitizer modality for cancer therapy.

2 Experimental

2.1 Chemicals, lipids, reagents, and antibodies

1,2-Dipalmitoyl-sn-glycero-3-phosphocholine (DPPC), 1-palmitoyl-2-[6-[(7-nitro-2-1,3-benzoxadiazol-4-yl)amino]hexanoyl]-sn-glycero-3-phosphocholine (NBD-PC), and 3 β -[N-(N',N'-dimethylaminoethane)-carbamoyl]cholesterol (DC-chol) were purchased from Avanti Polar Lipids (Alabaster, AL). L- α -phosphatidylethanolamine, distearoyl methoxypolyethylene glycol conjugate (DSPE-PEG, average PEG molecular mass of 2,000 amu), ZnPC (97% purity), 4-(2-hydroxyethyl)-1-piperazineethanesulfonic acid (HEPES), fibronectin, sodium chloride (NaCl), Triton X-100, cholesterol, chloroform, Nile Red, paraformaldehyde, sucrose, bovine serum albumin (BSA), Tween 20, CoCl₂, ACF, sulforhodamine B (SRB), trichloroacetic acid, TRIS, tirapazamine (TPZ), and pyridine were obtained from Sigma-Aldrich (St. Louis, MO). Tris-HCl and DMSO were acquired from Merck KgaA (Darmstadt, Germany). Methanol and ethanol were obtained from Biosolve (Valkenswaard, the Netherlands). Water-soluble tetrazolium-1 (WST) and RNase A were purchased from Roche Applied Science (Basel, Switzerland). Mouse anti-human HIF-1 α antibodies (clone 54/HIF-1 α) were from BD Transduction Laboratories (Franklin Lakes, NJ), mouse anti-human β -actin antibodies (AC-74) were from Sigma-Aldrich, and mouse anti-human phospho-H2AX-AlexaFluor647 antibodies were from Cell Signaling Technology (Danvers, MA).

Horseradish peroxidase-labeled polyclonal goat-anti-mouse IgG₁ secondary antibodies were from Dako Cytomation (Glostrup, Denmark). Sephadex G50 fine was from GE Healthcare (Piscataway, NJ).

All (derivatized) lipids were dissolved in chloroform, purged with nitrogen gas, and stored at -20°C . Phospholipid stock concentrations were determined by the inorganic phosphate assay modified from Ref. [37]. ZnPC was dissolved in pyridine to a concentration of 178 μM and stored at room temperature (RT) in the dark. ACF was dissolved in methanol up to a stock concentration of 1 mM and TPZ was dissolved in DMSO to a stock concentration of 10 mM. CoCl₂ was dissolved in MilliQ water to a concentration of 50 mM and filter-sterilized (0.2 μm , Corning, Corning, NY). The physiological buffer (10 mM HEPES, 0.88% (*w/v*) NaCl, pH = 7.4, 0.292 osmol/kg) was prepared in MilliQ. Nile Red was dissolved in DMSO to a concentration of 5 mM.

2.2 Absorption and fluorescence spectroscopy

Absorption spectroscopy was performed using a Lambda Bio spectrophotometer (Perkin Elmer, Waltham, MA). Fluorescence excitation and emission spectra of ACF were recorded on a Cary Eclipse fluorescence spectrometer (Varian, Palo Alto, CA).

2.3 Preparation and characterization of liposomes

Liposomes composed of DPPC:DC-chol:cholesterol:DSPE-PEG (66:25:5:4 molar ratio, unless indicated otherwise) and ZnPC (ZnPC:lipid molar ratio of 0.003) were prepared by the lipid film hydration technique as described in Refs. [7] and [38]. The hydrated lipid film was bath-sonicated (60 $^{\circ}\text{C}$) and the resulting cationic liposomes (referred to as endothelium-targeting liposomes, ETLs) were stored under nitrogen gas at 4 $^{\circ}\text{C}$ in the dark. The size and polydispersity of ZnPC-ETLs were characterized by photon correlation spectroscopy (Zetasizer 3000, Malvern Instruments, Malvern, Worcestershire, UK) using settings reported previously in Ref. [7]. Typically, ZnPC-ETLs had a diameter of 185.9 ± 8.3 nm, a polydispersity index (PDI) of 0.214 ± 0.05 , and a ζ -potential of 3.9 ± 1.2 mV. The lipid concentrations of the liposomal preparations were determined as described in section 2.1 and corrected for the (DC-)chol content based on predefined



molar ratios. Final lipid concentrations are given throughout the manuscript. At a constant ZnPC:lipid ratio of 0.003, the final ZnPC concentration is equal to $0.003 \times$ the final lipid concentration.

To investigate intraliposomal localization of ZnPC, ZnPC-encapsulating DPPC liposomes were prepared as described above and 0.1 mol% of Rho-PE was incorporated at the expense of DPPC. Due to the absence of PEGylation, liposomes tend to fuse directly after sonication and consequently increase in size. This enables their imaging by confocal fluorescence microscopy that was performed as described in section 2.14.

ACF-containing ZnPC-ETLs (ACF-ZnPC-ETLs) or ETLs without ZnPC (ACF-ETLs) were prepared by mixing ACF with lipids at predefined ratios and following the same preparation steps as described for ZnPC-ETLs. Non-encapsulated ACF was removed by size-exclusion chromatography. For this, 2.5 mL syringes were loaded with Sephadex G50 fine (GE Life Sciences, Pittsburgh, PA) that was equilibrated for >4 h in the physiological buffer (4 °C). The column was dried by centrifugation ($900 \times g$, 2 min, 4 °C). The liposomes were loaded onto the column (500 μ L loading volume) and eluted by centrifugation ($800 \times g$, 8 min, 4 °C). To determine encapsulation efficiency, 100 μ L of the liposomal suspensions was lysed in 900 μ L methanol: water (1:1 *v/v*) containing 0.1% Triton X-100. Then, the phospholipid content was determined as described in section 2.1 and the ACF content was measured by spectrofluorometry. Fluorescence emission spectra of the ACF-containing solution and ACF standards prepared in the same solvent was measured at $\lambda_{\text{ex}} = 415$ nm and $\lambda_{\text{em}} = 425$ –470 nm. The ACF concentration was derived by plotting the area under the emission curve and solving the second-order polynomial fit of the standard curve (range: 0–40 μ M).

For the liposomal stability assays, liposomes were prepared as described above and purged with N_2 or O_2 as indicated. The suspensions were stored in the dark at 4 °C. ZnPC absorption spectra were recorded in triplicate every 7 days to confirm the chemical integrity of ZnPC.

2.4 Oxidation assays

Generation of ROS *in vitro* during irradiation of ZnPC-ETLs was measured with the oxidation-sensitive fluorogenic probe 2',7'-dichlorodihydrofluorescein

(DCFH₂), which is oxidized to 2',7'-dichlorofluorescein (DCF) in the presence of ROS. DCFH₂ was prepared from DCFH₂-diacetate as described previously in Ref. [39]. The final concentration of DCFH₂ in DMSO was 3.6 mM. The DCFH₂ oxidation assay was performed as described previously in Ref. [7]. In short, 1,186 μ L of physiological buffer was added to a quartz cuvette containing a magnetic stirrer, after which time-based acquisition of DCF emission ($\lambda_{\text{ex}} = 500 \pm 5$ nm, $\lambda_{\text{em}} = 525 \pm 5$ nm, 20 °C, constant stirring) was started in a spectrofluorometer. After initiation of time-based acquisition, 12 μ L of (ZnPC-)ETLs (final lipid concentration in the cuvette: 50 μ M), and 2 μ L of DCFH₂ (final concentration in the cuvette: 6 μ M) were added to the cuvette at 1-min intervals. At $t = 3$ min, the cuvette was irradiated for 2 min with a 671-nm solid-state diode laser (CNI Laser, Changchun, China) at a light intensity of 500 mW. Time-based acquisition of DCF fluorescence emission was stopped at $t = 6$ min. The average fluorescence intensity during the last minute was corrected for the average fluorescence intensity during the third minute (background fluorescence).

The oxidation of tryptophan (Trp) residues in BSA was determined as a measure of protein oxidation as described previously in Ref. [7]. The BSA oxidation assay solution consisted of 0.1% BSA, 0.88% NaCl, and 10 mM HEPES (pH = 7.4). An assay solution volume of 1,080 μ L was added to a quartz cuvette with a magnetic stirrer. The fluorescence intensity of Trp was monitored using time-based acquisition in a spectrofluorometer at $\lambda_{\text{ex}} = 288 \pm 5$ nm, $\lambda_{\text{em}} = 340 \pm 5$ nm, and 20 °C under constant stirring. At $t = 1$ min, 60 μ L of the (ZnPC-)ETL solution was added to the cuvette. At $t = 2$ min, the cuvette was irradiated for 2 min with a 671-nm laser with a power output of 500 mW. Time-based acquisition was stopped at $t = 5$ min. The average fluorescence intensity at $t = 5$ min was corrected for background fluorescence ($t = 2$ min).

2.5 Cell culture

A431 cells were cultured under standard conditions (humidified atmosphere containing 95% air and 5% CO_2 , 37 °C) in phenol red-containing Dulbecco's modified Eagle's medium (DMEM, Gibco/Life Technologies, Gaithersburg, MD) supplemented with 4 mM L-glutamine, 10% fetal bovine serum (FBS, Gibco),

and penicillin/streptomycin (Lonza, Basel, Switzerland, 50 U/mL each). The cells were subcultured once a week at a 1:25 ratio and seeded in 24- or 6-well plates (Corning) at a density of 2×10^5 cells/mL and 500 μ L medium/well (24-well plates) or 1.5 mL/well (6-well plates).

Cells were maintained at standard normoxic (95% air, 5% CO₂, 37 °C) or at hypoxic culture conditions (<1% O₂, 5% CO₂, 37 °C using a gas mixture of 95% nitrogen, 5% CO₂ (Linde Gas, Schiedam, the Netherlands)). Hypoxic culture conditions were achieved in a custom-built air-tight plastic incubator (11.6 in. \times 9.1 in. \times 5.4 in.) comprising a gas inlet, a gas outlet connected to a bubble trap, a temperature regulation system (silicone tubing), closed loop system connected to a dual temperature circulator (model TLC 3, Tamson Instruments, Bleiswijk, the Netherlands), a metal grid for placement of the multiwell plate, wetted gauze in a petri dish to obtain 99% humidity, and a 2-in. computer fan secured to the metal grid for homogenous gas distribution. The O₂ fraction in the chamber was measured with an OdaLog gas monitor (App-Tek International, Brendale, Australia). The temperature inside the incubator was continuously monitored using a wireless thermometer (Oregon Scientific, Tualatin, Oregon).

2.6 Liposome uptake assays

Fluorescently labeled liposomal formulations were prepared for the uptake assays, in which 4% NBD-PC replaced DPPC. A431 cells were seeded as described in section 2.5 and grown to subconfluence overnight. Cells received fresh, serum-free medium in which 100 μ M (final lipid concentration) NBD-ETLs were suspended. Cells were incubated for 24 h and washed three times with 1 mL of phosphate-buffered saline (PBS). NBD fluorescence was measured using a BioTek multiplate reader (BioTek, Winooski, VT) at $\lambda_{\text{ex}} = 460 \pm 40$ nm, and $\lambda_{\text{em}} = 520 \pm 20$ nm. Data were corrected for background fluorescence (control cells).

For the ACF-ETLs, cells were seeded and grown to confluence as described in section 2.5. Uptake of 0–500 μ M ACF-ETLs was determined following 12 h of incubation in the dark under standard culture conditions. Subsequently, cells were washed twice with 1 mL of PBS, after which 300 μ L of PBS was added to

each well. ACF fluorescence was measured using the same settings as described above for NBD. Following fluorescence spectroscopy, cells were fixed in ice-cold trichloroacetic acid and total protein levels were determined using the sulforhodamine B method (described in section 2.8).

2.7 Photodynamic therapy

Prior to PDT, the culture medium was removed and cells were washed once with 1 mL of PBS (RT). Cells received fresh, serum-free medium supplemented with ZnPC-ETLs at concentrations indicated separately in the Results section. The cells were incubated for 1 h at standard culture conditions, washed twice with 1 mL of PBS (RT), and supplemented with fresh serum- and phenol red-free medium. Subsequently, PDT was performed at RT with a 671-nm solid state diode laser (CNI Laser) at a power of 500 mW. The spot size and duration of irradiation were adjusted to the surface of a single well (1.9 cm², 57 s) or a 6-well plate (9.5 cm², 285 s) to achieve a cumulative radiant exposure of 15 J/cm².

Cells were treated by PDT as follows. On day 0, cells were seeded as described in section 2.5 and allocated to the control group (CTRL), ACF group (ACF preconditioning only), PDT group (PDT only), or ACF + PDT group (ACF preconditioning followed by PDT). On day 1, cells received serum-free medium (CTRL and PDT groups) or serum-free medium containing 3 μ M ACF. On day 2, the medium was removed and cells received fresh, serum-free culture medium (CTRL and ACF groups) or serum-free medium containing 10 μ M ZnPC-ETLs (final lipid concentration, PDT and PDT + ACF groups). Cells were incubated with ZnPC-ETLs for 1 h at standard culture conditions and irradiated as described above. Subsequently, cells were kept at standard culture conditions for 4 h, i.e., at normoxia. Alternatively, cells were photosensitized with 5 μ M ZnPC-ETLs for 1 h, irradiated, and subsequently maintained for 4 h under hypoxic culture conditions to mimic vascular shutdown conditions post-PDT.

2.8 Cell viability assays

Cell viability was determined using the water-soluble tetrazolium-1 (WST-1) method as described in Ref. [7].

Where indicated, cell viability was assayed using the SRB protein assay as described in Ref. [40]. SRB absorption was read at 564 nm and corrected for absorbance at 690 nm (reference wavelength) using a multi-well plate reader (BioTek).

2.9 Immunoblotting

A431 cells were seeded in 6-well plates (section 2.5). After 24 h, cells were incubated with 10 μ M ZnPC-ETLs (final lipid concentration) and treated with PDT (section 2.7). At predefined time points after PDT, cells were placed on ice and immediately lysed in the ice-cold Laemmli buffer (for composition, see Cold Spring Harbor recipes for 2 \times Laemmli buffer) supplemented with a protease inhibitor cocktail (1 tablet per 5 mL buffer, Roche Applied Science). As a positive control for HIF-1 α stabilization, cells were incubated with 500 μ M CoCl₂ for 20 h prior to lysis [24]. The lysates were passed ten times through a 25-gauge needle (BD Biosciences, San Jose, CA) to mechanically shear DNA. Next, samples were incubated at 95 °C for 10 min and centrifuged at 13,000 \times g for 15 min at 4 °C. Proteins (30 μ g) were separated on 10% sodium dodecyl sulfate polyacrylamide gel electrophoresis (SDS-PAGE) precast gels (50 μ L slot volume, Bio-Rad Laboratories, Hercules, CA) for 90 min at 125 V. Subsequently, the gels were blotted onto PVDF membranes (Millipore, Billerica, MA) that had been primed in methanol for 10 min.

Blotting was performed for 1 h at 330 V at 4 °C. Protein membranes were blocked for 1 h in Tris-buffered saline (TBS, 20 mM Tris-HCl, 150 mM NaCl, pH = 7.5) with 0.2% Tween 20 (TBST) supplemented with 5% dried milk powder (Protifar, Nutricia, Cuijk, the Netherlands). Next, the membranes were incubated with antibodies (anti-HIF-1 α 1:500, anti- β -actin 1:4,000) for 16 h at 4 °C on a rocker, washed four times in TBST, and incubated with secondary antibodies (goat- anti-mouse, 1:1,000) for 1 h at RT. Membranes were washed three times in TBST and twice in TBS. Detection of β -actin was performed with an enhanced chemiluminescence (ECL) kit (Thermo Scientific), while detection of HIF-1 α was performed with the ECL plus reagent (Thermo Scientific) on an ImageQuant LAS 3000 luminometer (GE Healthcare).

2.10 Quantitative reverse transcriptase polymerase chain reaction (qRT-PCR)

RNA extraction from cells seeded in 6-well plates was performed by lysing cells in 0.5 mL TRIzol according to the manufacturer's protocol (Life Technologies). RNA was quantified with a Nanodrop 2000 UV-VIS spectrophotometer (Thermo Scientific) and checked for genomic DNA contamination (A260/A280 ratio \geq 1.80). Reverse transcription of 1 μ g of total RNA was performed using oligo-dT primer and the forward primer of S18 rRNA (Table 1). cDNA was synthesized

Table 1 Primer pairs sequences used for qRT-PCR

Gene	Forward primer sequence	Reverse primer sequence
<i>HIF1A</i>	GCGCGAACGACAAGAAAAAGA	CCAGAAGTTTCCTCACACGC
<i>BCL2</i>	TTTGTGGAAGTGTACGGCCC	CAGCCTGCAGCTTTGTTTCA
<i>BECN1</i>	ATCTGCGAGAGACACCATCC	TGTCACCATCCAGGAACCTCA
<i>BIRC5</i>	AGGACCACCGCATCTCTACA	TGTTCTCTATGGGGTCGTCA
<i>EDN1</i>	GGGCTGAAGGATCGCTTTGA	GCGCCTAAGACTGCTGTTTC
<i>HK1</i>	CGCAGCTCCTGGCCTATTAC	CATGATTCACTTGCACCCGC
<i>HMOX1</i>	AGGGAATTCTCTTGGCTGGC	GCTGCCACATTAGGGTGTCT
<i>HSPA5</i>	GGCATCGACCTGGGGACCAC	TCATTCCACGTGCGGCCGAT
<i>LDHA</i>	GACGTCAGCATAGCTGTTCCA	GCAAGTTCATCTGCCAAGTCC
<i>PDHA</i>	GGAGGCCGGCATCAACC	TTAGCAGCACCATCGCCATA
<i>PGK1</i>	CCCTCGTTGACCGAATCACC	CAGCAGCCTTAATCCTCTGGTT
<i>PKM2</i>	GGGTTCGGAGGTTTGATG	ACGGCGGTGGCTTCTGT
<i>PTGS2</i>	GGCCATGGGGTGGACTTAAA	CCCCACAGCAAACCGTAGAT
<i>SERPINE1</i>	ATGCCCTCTACTTCAACGGC	TTCCAGTGGCTGATGAGCTG
<i>VEGF</i>	CCACACCATCACCATCGACA	CTAATCTTCCGGGCTCGGTG
<i>S18 rRNA</i>	TTCGGAAGTGAAGCCATGAT	CGAACCTCCGACTTTCGTTCT

using a Superscript reverse transcriptase kit according to the manufacturer's protocol (Roche). Primers (Biolegio, Nijmegen, The Netherlands) for each target gene were designed using the NCBI primer design tool (Table 1). qRT-PCR was performed with Sensifast SYBR green (Bioline, London, UK) on 25 ng of cDNA using primers at a final concentration of 500 nM in a reaction volume of 10 μ L. The qRT-PCR run program comprised 3 min at 95 °C, 45 cycles of 1 s at 94 °C, 7 s at 65 °C, and 10 s at 72 °C, followed by melting curve analysis (65–97 °C in 60 s, 4 °C ∞) (LightCycler 480, Roche). Each primer pair in Table 1 was designed to allow transcript variant amplification and passed several quality checks (PCR efficiency (typically >80%), single-amplicon melting curve, and correct amplicon size). Data analysis was performed using LinReg as described in Ref. [41]. A \log_2 transformation was performed in order to obtain absolute fold-differences in expression levels of the genes of interest.

2.11 Molecular docking

The X-ray structure of the ligand-bound Per-Arnt-Sim (PAS) domain was retrieved from the Protein Data Bank (<http://www.rcsb.org>). The search yielded the following structure/ligand combinations: 3F1O/2XY, 3H7W/018, 3H82/020, and 4GHI/0X3. Molecular docking calculations were carried out using the AutoDock Vina software [42]. Ligand structures were optimized using the Dreiding force field [43] implemented in the Molconvert software (Chemaxon, Budapest, Hungary). Gasteiger partial charges [44] were calculated on ligand atoms. Polar hydrogen atoms were added to the protein and Gasteiger partial charges were calculated using AutoDock Tools. Water molecules and heteroatoms were removed from the structures. Simulation boxes were centered on the originally crystallized ligands. A 20 Å \times 20 Å \times 20 Å simulation box was used in each docking calculation with an exhaustiveness option of 8 (average accuracy).

A new term was introduced into the AutoDock Vina scoring function that enables the addition of a distance-dependent restrain for a given interaction between a ligand atom type and a specific protein atom. The AutoDock Vina source code was modified accordingly and an executable file was generated using gcc. The restrain was defined as a hydrogen bond

donor atom type of the ligand and the NH backbone atom of the critical residue, being minimized at –5 kcal/mol. The restrained bonding distance had a cut-off value of 4 Å.

Re-docking experiments on the retrieved PAS domain/ligand structures were performed to assess the predictive power of the general scoring function implemented in AutoDock Vina. The experimental complex geometry could be fully reproduced with the docking calculations using the general scoring function. Thus, no further refinement of the scoring function was implemented.

2.12 Caspase 3/7 activity

Cells were seeded and subjected to PDT as described in section 2.5 and 2.7, respectively. Following PDT, cells were cultured in 200 μ L of serum- and phenol-red free medium and maintained at either normoxic or hypoxic conditions for 3.5 h post-treatment. Subsequently, 25 μ L of the Caspase-Glo assay reagent (Promega, Madison, WI) was added and cells were incubated for 30 min at standard culture conditions. Luminescence was read on a Synergy HT multiplate reader (BioTek) at 560 \pm 20 nm and a signal integration time of 1 s. Data was obtained from 5 measurements and corrected for background luminescence.

2.13 Extracellular lactate determination

Extracellular lactate levels were studied by using the EDGE blood lactate analyzer (Apex Biotechnology, Hsinchu, Taiwan). Lactate concentrations were determined using a standard curve of lactate in phenol red-free DMEM and corrected for the average protein content/group to adjust for the toxicity of the treatment.

2.14 Confocal laser scanning microscopy

All cells and ZnPC-containing DPPC liposomes were imaged on a Leica SP8 laser scanning confocal microscopy system (Leica Microsystems, Wetzlar, Germany).

Intracellular localization of ACF and occurrence of DNA damage were investigated before and after PDT using confocal laser scanning microscopy. Microscope cover slips (24 mm \times 40 mm, VWR, Lutterworth, UK) were placed in 6-well plates and coated with (5 \times 10^{–4}%) (*w/v*) fibronectin in 1 mL of sterile 0.9% NaCl solution



(Fresenius Kabi, Bad Homburg, Germany) for 2 h at 37 °C prior to cell seeding. The fibronectin-containing solution was removed and the cells were seeded onto the cover slips (densities specified in section 2.5) and incubated overnight.

For the ZnPC uptake experiment, cells were incubated for 4 h with 100 μ M ETLs in which ZnPC was encapsulated at a ZnPC:lipid ratio of 0.024. Cells were subsequently incubated with 50 nM Mitotracker Red (MTR, Life Technologies, Carlsbad, CA) for 30 min at standard culture conditions. After incubation, cells were washed with 1 mL of PBS (RT) and fixed in 4% paraformaldehyde/0.2% sucrose for 5 min, after which the coverslips were mounted on microscope slides using the Vectashield mounting medium (Vector Laboratories, Burlingame, CA).

For the ACF uptake experiment, cells were subjected to PDT (section 2.7) and subsequently incubated with 3 μ M ACF for 4 h at normoxic or hypoxic conditions as indicated. After incubation, cells were washed with 1 mL of PBS (RT) and fixed in 4% paraformaldehyde/0.2% sucrose for 5 min. After fixation, cells were washed with 1 mL of PBS (RT). Nile Red staining was performed with 1 μ M Nile Red in PBS for 60 s. Cells were washed three times with 1 mL PBS and mounted on microscope slides using the Vectashield mounting medium.

For DNA damage assessment, cells were permeabilized after fixation by 5-min incubation in 1 mL PBS containing 0.1% Trion X-100 (RT). Cells were washed with 1 mL of PBS (RT), after which they were incubated with mouse-anti-human phospho-H2AX-AlexaFluor647 at a 1:100 dilution in 0.5% BSA and 0.15% glycine in PBS (staining buffer) for 16 h at 4 °C. Cells were washed three times with the staining buffer and subsequently mounted on microscope slides using Vectashield mounting medium with 4',6-diamidino-2-phenylindole (DAPI) (Vector Laboratories). Slides were dried for 1 h and sealed with nail polish.

To determine intraliposomal ZnPC localization, ZnPC-encapsulating liposomes were prepared as described in section 2.3. Next, 9.5 μ L of Vectashield mounting medium was placed on a microscope slide and 0.5 μ L of 200 μ M (final lipid concentration) liposome suspension was resuspended in the mounting medium. A coverslip was placed on top of the

microscope slide that was sealed with nail polish.

Fluorescence was measured at $\lambda_{\text{ex}} = 405$ nm, $\lambda_{\text{em}} = 415$ –480 nm for DAPI, $\lambda_{\text{ex}} = 470$ nm, $\lambda_{\text{em}} = 480$ –550 nm for ACF, $\lambda_{\text{ex}} = 540$ nm, $\lambda_{\text{em}} = 550$ –650 nm for Nile Red, $\lambda_{\text{ex}} = 540$ nm, $\lambda_{\text{em}} = 550$ –580 nm for Rho-PE, $\lambda_{\text{ex}} = 660$ nm, $\lambda_{\text{em}} = 670$ –750 nm for phospho-H2AX, and $\lambda_{\text{ex}} = 670$ nm, $\lambda_{\text{em}} = 680$ –730 nm for ZnPC. All experiments were performed using the same laser and microscope hardware settings. The mean phospho-H2AX fluorescence intensity per cell within each treatment group were analyzed with ImageJ (National Institutes of Health, Bethesda, MD). To generate a positive control for DNA damage, cells were subjected to a similar treatment as the ACF group, but ACF was replaced with TPZ, a DNA-oxidizing agent, at a final concentration of 50 μ M.

2.15 Statistical analysis

Data were analyzed using the GraphPad Prism software (GraphPad Software, San Diego, CA). Data were initially checked for normality using the Kolmogorov-Smirnov test. Normally distributed data sets were analyzed with either the Student's *t*-test or one-way ANOVA followed by a Tukey's post hoc test, if appropriate. All data are reported as mean \pm standard deviation. In the figures, significant intergroup differences are indicated with (*), differences between treated groups versus the untreated (CTRL) group are indicated with (#), and differences between normoxic and hypoxic data are indicated with (\$). The level of significance of differences is indicated by a single ($P < 0.05$), double ($P < 0.01$), triple ($P < 0.005$), or quadruple sign ($P < 0.001$).

3 Results and discussion

3.1 Characterization of ZnPC-ETLs

Several studies have shown the ability of cationic liposomes to target tumor vasculature [13, 45, 46]. PEGylation is essential in order to prevent uptake of these liposomes by non-target cells, bestow long-circulating capacity, and minimize adverse events *in vivo* caused by toxicity of cationic lipids (reviewed in Ref. [11]). Although liposomes that contain ZnPC have been developed by us [7] and others [47, 48],

photosensitizer-containing cationic liposomes have been rarely used in conjunction with cancer treatment by PDT [49]. Consequently, a cationic liposomal formulation for the delivery of ZnPC to tumor cells *in vitro* and the tumor vasculature *in vivo*, which has been developed previously [7], was investigated further in the present study.

In the first set of experiments, the effects of cationic lipid DC-chol on the liposome characteristics and

photodynamic efficiency of encapsulated ZnPC were investigated. Liposomes with a higher DC-chol content exhibited a higher ζ -potential (Fig. 2(a)), which could be reduced by inclusion of 4 mol% DSPE-PEG in the lipid bilayer (Figs. 2(a) and 2(b)). Increasing the DSPE-PEG content beyond 4 mol% did not further reduce the ζ -potential of liposomes that contained 30 mol% DC-chol (Fig. 2(b)). The effect of DC-chol inclusion on PDT efficacy of co-encapsulated ZnPC is

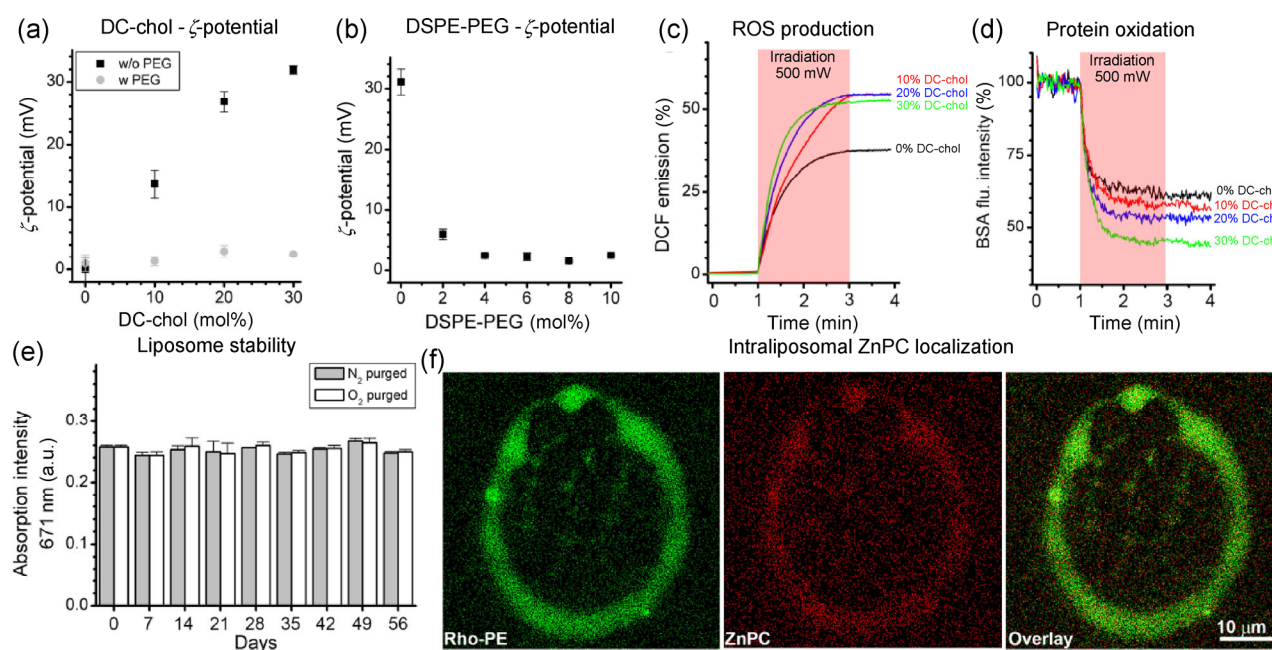


Figure 2 (a) The effect of increasing concentrations of DC-chol and PEGylation on the ζ -potential of ETLs as measured by electrophoretic light scattering. The basic composition of liposomes without DSPE-PEG (black squares) was DPPC:cholesterol (70:30), in which the indicated molar proportion (mol%) of DC-chol was included at the expense of cholesterol. The basic composition of liposomes with DSPE-PEG (gray dots) was DPPC:cholesterol:DSPE-PEG (66:30:4), in which the indicated mol% of DC-chol was included at the expense of cholesterol. (b) The effect of DSPE-PEG content on the ζ -potential of ETLs composed of DPPC:DC-chol (70:30), where the indicated mol% of DSPE-PEG was included at the expense of DPPC. The depicted results represent the mean of 3 measurements in which the ζ -potential was measured 5 times for 20 s. Statistical analysis was performed using the unpaired Student's *t*-test, asterisks indicate $P < 0.05$. (c) Traces of DCF fluorescence emission intensity are depicted for liposomes with increasing DC-chol content. Liposomes were composed of DPPC:cholesterol:DSPE-PEG (66:30:4, black line), DPPC:cholesterol:DC-chol:DSPE-PEG (66:20:10:4, red line), DPPC:cholesterol:DC-chol:DSPE-PEG (66:10:20:4, blue line), or DPPC:DC-chol:DSPE-PEG (66:30:4, green line). During time-based acquisition, DCFH₂ was added to the cuvette at $t = -1$ min and the liposomes were added at $t = 0$ min. Laser irradiation of the cuvette (500 mW, 671 nm) was performed at $t = 1$ –3 min (semi-opaque red rectangle). (d) Traces of BSA fluorescence emission intensity are depicted for liposomes with increasing DC-chol content. Liposomes were composed of DPPC:cholesterol:DSPE-PEG (66:30:4, black line), DPPC:cholesterol:DC-chol:DSPE-PEG (66:20:10:4, red line), DPPC:cholesterol:DC-chol:DSPE-PEG (66:10:20:4, blue line), or DPPC:DC-chol:DSPE-PEG (66:30:4, green line). During time-based acquisition, the BSA assay solution was added at $t = -1$ min, liposomes were added at $t = 0$ min, and the cuvette was irradiated (500 mW, 671 nm) at $t = 1$ –3 min (semi-opaque red rectangle). Traces were normalized to the mean fluorescence intensity at $t = 0$ –1 min. (e) The stability of ZnPC-ETLs (DPPC:cholesterol:DC-chol:DSPE-PEG, 66:5:25:4, ZnPC:lipid ratio, 0.003) as measured by the absorption at 671 nm (ZnPC Q-band maximum) during a period of 56 days ($N = 3$ per time point). (f) Confocal laser scanning microscopy of ZnPC-encapsulating DPPC liposomes in which 0.1 mol% Rho-PE was added at the expense of DPPC. Rho-PE is depicted in green. ZnPC is depicted in red. All images were obtained using a 63 \times oil immersion objective and digital zoom.

summarized in Fig. 2(c), which shows that the DCFH₂ oxidation levels were higher in DC-chol-containing liposomes than in DC-chol-lacking liposomes. Notably, the increase in DCFH₂ oxidation did not depend on the concentration of DC-chol. Oxidation of Trp in BSA by ZnPC-containing liposomes, which led to abrogation of Trp fluorescence, occurred in a DC-chol concentration-dependent fashion (Fig. 2(d)). Although these results may be interpreted as increased photodynamic efficacy, they may also reflect an increased interaction between anionic DCFH₂ and BSA with the cationic liposomes. Nevertheless, such interaction may hold biological significance due to intra- and extracellular abundance of anionic protein residues (e.g., Asp, Glu) and anionic membrane constituents (e.g., phosphatidylserine) in an *in vivo* setting [45, 50, 51]. Taken together, the results demonstrated that photodynamic activity of ZnPC-ETLs was not negatively affected by DC-chol.

To determine the stability of ZnPC in ZnPC-ETLs with respect to its physicochemical properties, oxidation of ZnPC was investigated in ZnPC-ETLs (0.003 ZnPC: lipid ratio, 25% DC-chol, 4% DSPE-PEG) by measuring the intensity of its absorption maximum at 671 nm as a function of time and oxygen tension. Accordingly, ZnPC-ETLs were purged with either N₂ gas or O₂ gas prior to storage. The results presented in Fig. 2(e) show that the spectral properties (i.e., chemical structure) of ZnPC remained unchanged throughout the experiment, regardless of O₂ presence. ZnPC-ETLs are therefore stable over a period of 56 days in terms of ZnPC structural integrity, which is required for ROS generation.

Given that ZnPC is hydrophobic ($\log P \sim 8$), it is assumed that it is readily incorporated into the lipid bilayer during the preparation procedure. To confirm this hypothesis, giant unilamellar vesicles were prepared using the standard ZnPC-ETL formulation containing 0.5 mol% Rho-PE, but without PEGylation. Subsequently, the liposomes were imaged with confocal fluorescence microscopy and colocalization of ZnPC with fluorescently labeled lipids was revealed (Fig. 2(f)).

3.2 Uptake of ZnPC-containing cationic liposomes

To determine the most suitable lipid composition of the ETLs with respect to uptake, 4 different liposomal formulations were prepared, characterized, and tested.

Figure 3(a) provides an overview of the composition, size, polydispersity indices, and ζ -potentials of these liposomal preparations. Whereas DC-chol-lacking liposomes sterically stabilized with 4% DSPE-PEG (formulation 1) had a relatively neutral ζ -potential of 0.9 ± 0.2 mV, inclusion of 25% DC-chol in the absence of DSPE-PEG conferred a considerably more positive ζ -potential on the liposomes (formulation 2, 29 ± 1.4 mV). However, the ζ -potential was reduced upon co-incorporating 4% DSPE-PEG into the lipid bilayer (formulation 3, 3.9 ± 1.2 mV). Further reduction in the ζ -potential was achieved after inclusion of 10% DSPE-PEG (formulation 4, 1.1 ± 0.3 mV).

Uptake of ZnPC-ETLs by human cholangiocarcinoma (Sk-Cha1) cells has been previously demonstrated by flow cytometry, which proved that cationic liposomes are taken up more intensively than neutral liposomes (formulation 1), despite inclusion of DSPE-PEG and thus a relatively lower ζ -potential [7] compared to that in non-PEGylated liposomes (formulation 2). In this study, the uptake of the neutrally charged PEGylated liposomes (formulation 1), cationic non-PEGylated liposomes (formulation 2), cationic PEGylated liposomes (formulation 3), and cationic highly PEGylated liposomes (formulation 4) was tested in A431 cells. Formulations 2 and 3 were taken up by A431 cells in larger amounts than formulation 1 (Fig. 3(b)). Increasing the DSPE-PEG content to 10% (formulation 4) reduced cellular uptake despite the presence of 25% DC-chol. Thus, the balance between cationic lipid content and the extent of PEGylation is essential for liposomal uptake kinetics. All subsequent experiments with ZnPC-ETLs were therefore performed with formulation 3 (hereafter abbreviated as “ZnPC-ETLs”), given its high uptake efficiency, steric stability due to the presence of PEG, and lower ζ -potential that minimizes adverse events *in vivo* [11].

The intracellular localization of a photosensitizer determines its mechanism of action in terms of PDT efficacy and the mode of cell death [37]. Therefore, the intracellular fate of ETL-delivered ZnPC was investigated in A431 cells. In accordance with the lipophilicity of ZnPC (Fig. 2(f)), A431 cells displayed intense ZnPC fluorescence emanating from the cytoplasmic membranes (Fig. 3(c)). ZnPC localized at distinct intracellular foci that were not mitochondria,

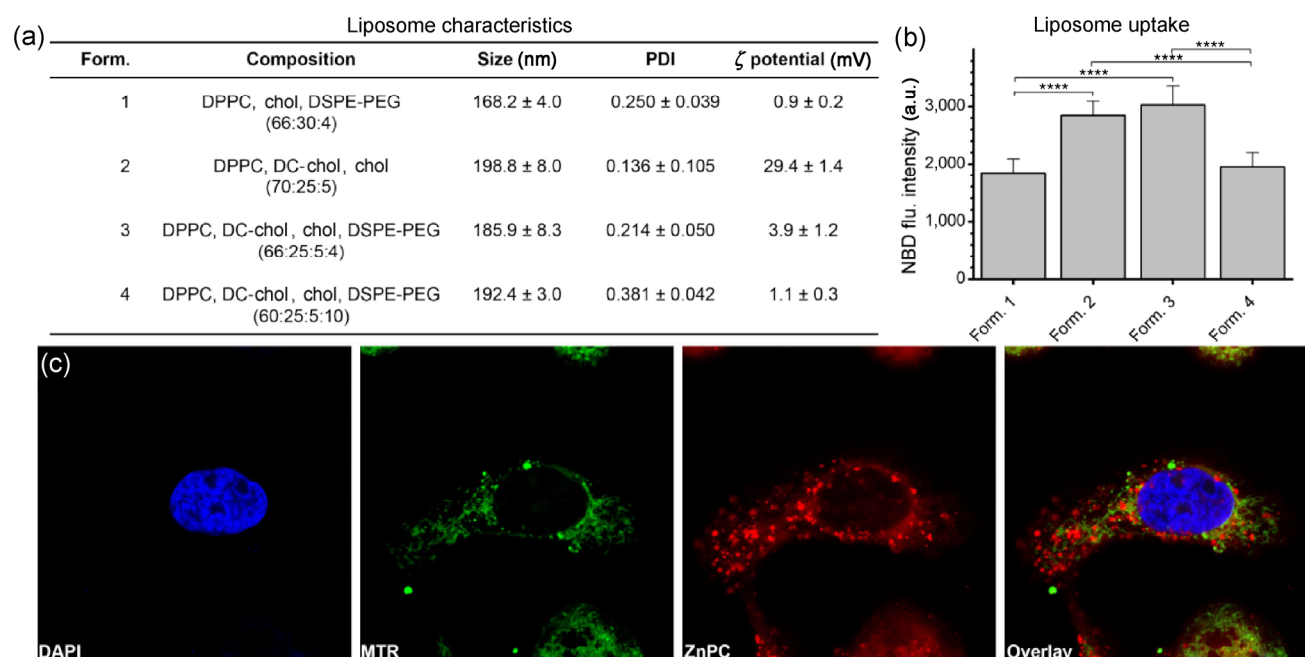


Figure 3 (a) Liposome characteristics of four liposomal formulations that were used for uptake analysis. (b) Uptake of NBD-labeled liposomes as a function of DC-chol and DSPE-PEG content. NBD fluorescence was measured after 24 h of incubation under standard culture conditions ($N = 9$). (c) Confocal laser scanning microscopy of A431 cells incubated for 1 h with ZnPC-ETLs (formulation 3, ZnPC:lipid ratio of 0.024, ZnPC fluorescence in red), counterstained with DAPI (blue) and MitoTracker Red (MTR, green). Images were obtained using a 63 \times oil immersion objective and digital zoom.

suggesting redistribution of ZnPC across organellar membranes following internalization of the liposomes.

3.3 Dark toxicity and PDT efficacy of ZnPC-ETLs

Prior to assessing the effects of PDT on HIF-1 activation, cytotoxicity of PDT with ZnPC-ETLs was determined. There was no cytotoxicity of ZnPC-ETLs up to a final lipid concentration of 50 μ M measured after a 24-h incubation period in the absence of light (Fig. 4(a)). PDT (15 J/cm²) resulted in a ZnPC concentration-dependent decrease in relative cell viability after 24 h of normoxic incubation (Fig. 4(b)). However, HIF-1 stabilization did not occur when cells were kept under normoxic conditions after PDT (data not shown). Thus, photochemical production of ROS and the short period of hypoxia induced by the conversion of O₂ to ROS are therefore not sufficient to stabilize HIF-1 α . Consequently, the experiments were also performed under hypoxic culture conditions to mimic vascular shutdown following PDT.

Under hypoxic conditions, A431 cells were more susceptible to PDT-induced cell death, as evidenced

by almost the same extent of cell death observed at a photosensitizer concentration that was \leq 50% the concentration used in the normoxia groups (Fig. 4(b)). Approximately 50% cell death was achieved with 10 and 5 μ M ZnPC-ETLs under normoxic and hypoxic conditions, respectively. Subsequent experiments regarding involvement of HIF-1 in the PDT response were therefore conducted using these final lipid concentrations.

3.4 Persistent HIF-1 α stabilization desensitizes A431 cells to PDT

Ji et al. showed that CoCl₂ treatment could desensitize Het1A esophageal tumor cells to PDT via upregulation of HIF-1 [24]. To investigate whether this phenomenon also occurs in A431 cells, susceptibility of A431 to PDT was determined after 24-h preconditioning with 500 μ M CoCl₂. Cells were subjected to PDT with 10 μ M ZnPC-ETLs (final lipid concentration), after which viability was measured at 4 h post-PDT ($N = 12$). CoCl₂ preconditioning significantly ($P < 0.001$) reduced PDT efficacy in A431 cells (Fig. 4(c)). Cells that were not

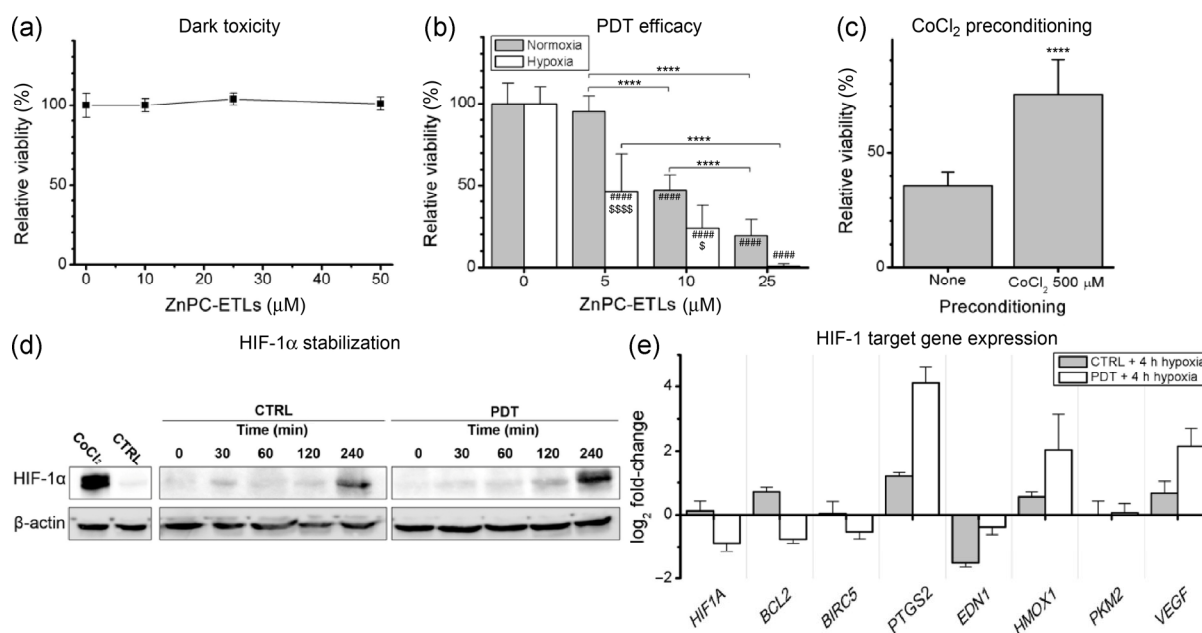


Figure 4 (a) Dark toxicity of ZnPC-ETLs after 24 h of incubation at the indicated concentrations ($N = 9$). (b) Viability of A431 cells subjected to PDT with increasing concentrations of ZnPC-ETLs. Viability was determined 24 h after PDT, during which cells were kept under either normoxic (gray bars) or hypoxic conditions (white bars) ($N = 6$). (c) Viability of A431 cells that were preconditioned with 500 μM CoCl_2 for 24 h under normoxic conditions and subsequently treated with PDT (10 μM ZnPC-ETLs). Viability was determined 4 h post-PDT ($N = 12$). (d) HIF-1 protein levels as determined by immunoblotting. Cells were incubated for 24 h with 500 μM CoCl_2 as a positive control for HIF-1 α stabilization. Cells were placed in hypoxic culture conditions for up to 240 min after undergoing no treatment (CTRL) or PDT (PDT, 10 μM ZnPC-ETLs, final lipid concentration). β -actin was used as a loading control. (e) qRT-PCR analysis of pertinent HIF-1-regulated genes after 4 h of hypoxic incubation (gray bars) or after PDT + 4 h of hypoxic incubation (white bars). Data ($N = 3$) are plotted relative to mRNA levels in untreated normoxic cells.

preconditioned with CoCl_2 exhibited a post-PDT viability of $36.6 \pm 6.0\%$, whereas cells that were preconditioned with CoCl_2 had a post-PDT viability of $75.4 \pm 14.9\%$. This was most likely the result of CoCl_2 -induced HIF-1 and HO-1 overexpression [24, 46, 47].

3.5 PDT exacerbates HIF-1 signaling

HIF-1 α stabilization did not occur under normoxic conditions (results not shown), which may be explained by a short half-life of HIF-1 α under normoxic conditions (~ 5 – 8 min, as reported in Ref. [48]). Under hypoxic conditions and in the absence of PDT, HIF-1 α expression stabilized from 30 min onwards. HIF-1 α stabilization was more pronounced following PDT under hypoxic conditions, whereby the extent of stabilization was proportional to the duration of hypoxia (Fig. 4(d)). The delay in the onset of hypoxic incubation and stabilization of HIF-1 α was most likely caused by a gradual depletion of residual O_2 in

the culture medium [49].

Several studies have investigated expression and activation of HIF-1 in the context of PDT. *In vitro*, chemically induced HIF-1 activation correlated positively with increased tumor cell survival post-PDT [24]. However, HIF-1 stabilization can occur in an oxygen-independent manner [19] and the degree of HIF-1 activation differs between cell lines [20]. *In vivo*, PDT has been shown to induce HIF-1 α stabilization and elevate vascular endothelial growth factor (VEGF) protein levels in a murine model of Kaposi's sarcoma [22]. In order to establish whether PDT has an auxiliary effect on HIF-1 activation in comparison to hypoxia alone in A431 cells, the expression of pertinent and frequently used reporter genes for HIF-1 activity [17, 34, 52–54] was determined. As shown in Fig. 4(e), the most prominent effects of PDT on HIF-1 target genes included higher expression of prostaglandin synthase 2 (PTGS2, COX-2), heme oxygenase 1

(*HMOX1*, HO-1), and VEGF receptor, reduced down-regulation of endothelin 1 (*EDN1*), and a decrease in the expression of *HIF1A* and b-cell lymphoma 2 (*BCL2*). The fold change in expression levels of survivin (*BIRC5*) and pyruvate kinase muscle 2 (*PKM2*) was <1.

The findings concerning changes in HIF-1 expression in A431 cells were in agreement with the previously discussed *in vitro* [19, 20, 24] and *in vivo* studies [21–23, 55]. The *in vivo* studies demonstrated that HIF-1 was stabilized in hypoxic tumor tissues as a result of vascular shutdown following PDT, which led to an increase in mRNA levels of *HIF1A*, *VEGF*, and *PTGS2* [55].

3.6 ACF binds to the dimerization domain of HIF-1 α

Inhibition of the function of proteins that are produced downstream of HIF-1 signaling was associated with increased PDT efficacy. For example, inhibition of VEGF with bevacizumab was shown to improve PDT outcome [22]. The same trend has been observed in experiments with BA mouse mammary carcinomas, which exhibited HIF-1 α stabilization and increased levels of survival and VEGF protein expression following PDT [21, 23]. Moreover, tumor growth rate and overall survival of PDT-treated CNE2 xenografts in mice could be increased by blocking tyrosine kinase receptors [55], to which VEGF receptor belongs. These data attest that the HIF-1 signaling axis is an important regulator of PDT consequences. However, rather than inhibiting the downstream products of HIF-1, inhibition of HIF-1 itself is pharmacologically more sensible in terms of an optimal adjuvant effect on PDT efficacy because such a manipulation would simultaneously block all signaling pathways downstream of HIF-1.

Specific inhibition of HIF-1 by ACF has been previously attributed to its binding to the PAS domain of HIF-1 α and subsequent prevention of HIF-1 α /HIF-1 β dimerization. To corroborate those findings and to determine which residues are involved in ACF/HIF-1 α complex formation, molecular docking of ACF to the HIF-1 α PAS domain was performed. It should be noted that docking of ACF to the PAS domain of HIF-1 resulted in favorable binding only in the case of the 3H7W crystal structure [56], which can be explained by minute differences in side chain conformations of the

crystal structures. ACF and the binding site possessed excellent shape complementarity as revealed in the docking simulation (Fig. 5). The ligand of 3H7W in the original study was an aniline derivative with no specific hydrogen bonding capacity, indicating that shape complementarity is essential to accommodate planar molecules in case of this narrow, closed binding site. As illustrated in Fig. 5, the main driving force for complex formation is a π - π interaction with the aromatic pocket formed by Phe244, His248, Phe254, Tyr281, His293, and Tyr307 of the binding site. In addition, the amino group of ACF is in a hydrogen bond with Tyr306, potentially indicating the presence of a strong interaction.

3.7 ACF exacerbates tumor cell death *in vitro*

To determine the most suitable concentration of ACF for a combined treatment, concentration-dependent uptake and toxicity of ACF were assessed. Uptake was measured by utilizing the intrinsic fluorescent properties of ACF as depicted in Fig. 6(a). ACF uptake followed a linear pattern up to a concentration of 4 μ M (Fig. 6(b)). The toxicity of ACF was determined during a 24-h incubation period under either normoxic or hypoxic conditions. ACF became slightly toxic at

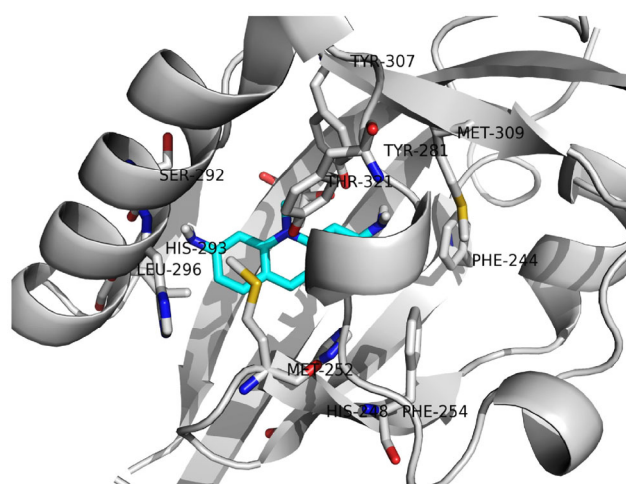


Figure 5 Orientation of ACF (cyan) in the PAS domain of HIF-1 α (3H7W crystal structure, gray) and its interaction with specific amino acid residues in the binding site. ACF binds to the PAS domain via a π - π interaction with the aromatic pocket formed by Phe244, His248, Phe254, Tyr281, His293, and Tyr307. Bonding is strengthened by a hydrogen bond between ACF amino group and Tyr306 (not shown).

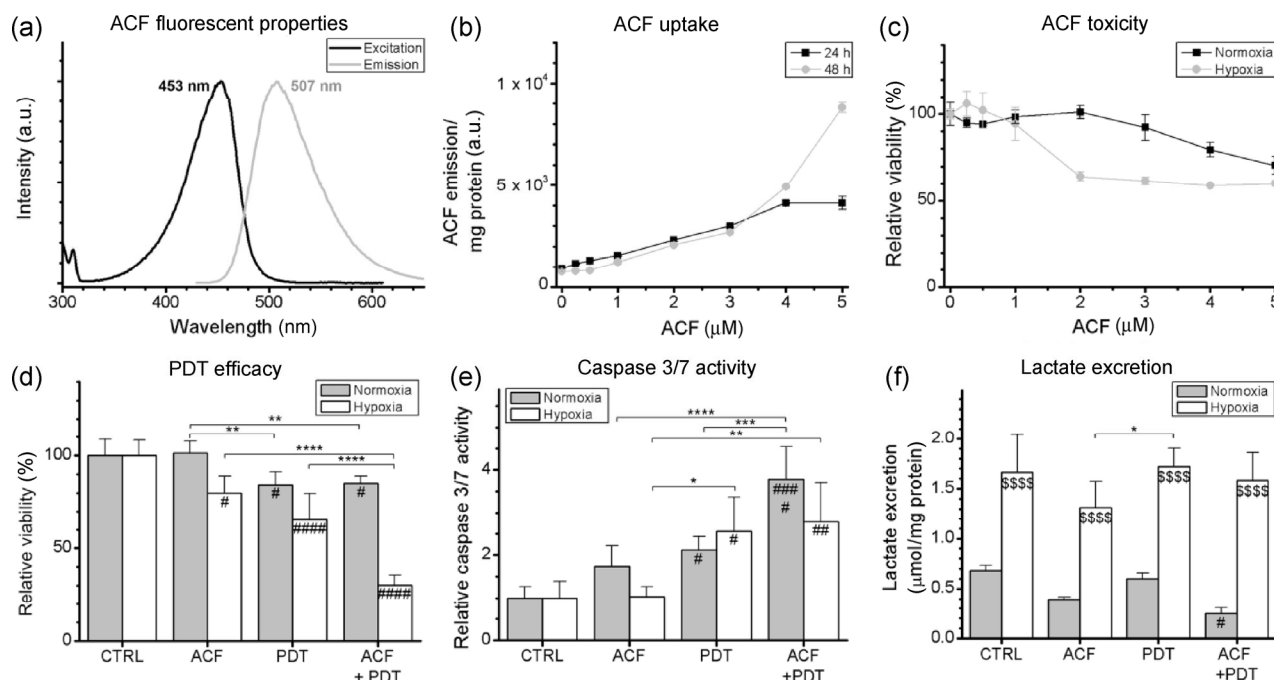


Figure 6 (a) Excitation (black line) and emission (gray line) characteristics of ACF in water. (b) The uptake of ACF was determined using fluorescence spectroscopy. Uptake was determined after 24 h of incubation at normoxic culture conditions. Data were normalized to protein content ($N = 3$). (c) Toxicity of ACF was determined after 24 and 48 h of either normoxic (black lines) or hypoxic culture conditions (gray lines). All data were normalized to the values measured in cells that were exposed to an equal volume of DMSO ($N = 3$). (d) PDT and neoadjuvant ACF treatment efficacy were tested after 4 h of normoxic incubation (gray bars) or hypoxic incubation (white bars) post-treatment ($N = 6$). (e) Relative caspase 3 and 7 activity was determined after PDT and 4 h of post-treatment incubation under normoxic (gray bars), or hypoxic conditions (white bars) ($N = 6$). (f) Levels of lactate excreted into the medium were determined in 24 h post-treatment after incubation under normoxic (gray bars) or hypoxic (white bars) conditions ($N = 6$).

concentrations of $>3 \mu\text{M}$ under normoxic conditions, with a 29% decrease in cell viability at $5 \mu\text{M}$ (Fig. 6(c)). Under hypoxic conditions, ACF decreased viability by $\sim 40\%$ at concentrations of $>1 \mu\text{M}$, but there was no further impact on viability of higher concentrations of ACF (Fig. 6(c)). Based on these data, ACF was used in further experiments at a concentration of $3 \mu\text{M}$.

Next, the neoadjuvant potential of ACF was investigated in terms of PDT efficacy. First, cells were preconditioned for 24 h with $3 \mu\text{M}$ ACF, treated by PDT with $10 \mu\text{M}$ ZnPC-ETLs, and kept under normoxic conditions. It was found that ACF alone did not induce any toxicity in A431 cells and did not impart an additional effect when used in conjunction with PDT (Fig. 6(d)). However, under hypoxic conditions, the extent of A431 cell death in the ACF + PDT group was more extensive than in the ACF group, indicating that ACF exerted an adjuvant effect on PDT efficacy (Fig. 6(d)).

To determine whether toxicity imparted by different treatments was mediated by apoptosis, the activity of caspases 3 and 7 was measured 4 h after each treatment. Under normoxic conditions, A431 cells did not exhibit a significant increase in apoptotic signaling following ACF treatment. After PDT, caspase 3/7 activity in treated cells was twice as high compared to control cells (Fig. 6(e)). Furthermore, a combined exposure to ACF and PDT resulted in 4-fold higher caspase 3/7 activity. Surprisingly, the adjuvant effect of ACF on PDT-induced apoptosis was abrogated in hypoxic A431 cells, indicating that the mechanisms of post-PDT cell death are dependent on ambient oxygen tension.

These results are in favor of the hypothesis that the beneficial effect of ACF on PDT outcome most likely stemmed from the downstream effects of HIF-1 α antagonism. One of the major functions of HIF-1 is stimulation of glycolysis over oxidative phosphorylation. In order to assess whether glycolysis was

upregulated in A431 cells by hypoxia, exacerbated by PDT, and inhibited by ACF, excretion of lactate was investigated. Lactate excretion by hypoxic cells was significantly higher than that by normoxic cells in all treatment groups (Fig. 6(f)). The combined application of ACF and PDT significantly lowered the extent of lactate production under normoxic conditions (gray bars). Under hypoxic conditions (white bars), the extent of lactate excretion was only affected by ACF but not by PDT alone or in combination with ACF. These results warrant further investigation regarding the role of glycolysis in the response to PDT.

Taken altogether, there was a significant increase in PDT efficacy when A431 cells were pretreated with ACF and subjected to post-therapeutic hypoxia. Although PDT induced cell death primarily through apoptosis, as shown by increased caspase 3/7 activity, the adjuvant effect of ACF on PDT efficacy did not correlate with that parameter, indicating that cells died via an alternative mechanism. In a previous study by Tennant et al., it was demonstrated that inhibition of HIF-1 activation by reactivation of PHDs with α -ketoglutarate under hypoxic conditions resulted in a metabolic catastrophe in HCT116 human colon carcinoma cells that was characterized by reduced glucose uptake, lowered lactate production, and a loss of plasma membrane functionality (i.e., programmed necrosis) [57]. Since A431 cells exposed to a combined treatment with ACF and PDT exhibited a similar pattern of reduced lactate production and increased caspase 3/7-independent cell death, our data corroborate the previous findings and suggest that A431 cells subjected to ACF + PDT perish as a result of a metabolic catastrophe with a necrotic phenotype. However, it should be noted that the hypoxia-induced increase in lactate production was hardly affected by PDT, implying that the HIF-1-induced metabolic switch from oxidative phosphorylation to glycolysis may not be an acute mechanism of cell survival following PDT.

3.8 ACF uptake and intracellular localization

Since ACF was readily taken up by A431 cells, uptake and intracellular localization of ACF were investigated with confocal laser scanning microscopy to determine its intracellular fate before and after PDT. ACF was imaged by utilizing its intrinsic fluorescent properties

(Fig. 6(a)). Nile Red, a lipophilic fluorogenic dye, was used to stain the membrane of paraformaldehyde-fixed cells and organelles. To observe intracellular ACF translocation as a result of PDT and/or altered oxygen tension, ACF was added to cells during hypoxic incubation and/or after PDT. Confocal images (Fig. 7) show that ACF did not abundantly localize to the endoplasmic reticulum (ER) and/or Golgi apparatus, given that the ACF fluorescence intensity was low in the perinuclear areas with intense Nile Red fluorescence. ACF fluorescence was not observed in defined intracellular foci, suggesting that ACF did not preferentially accumulate in mitochondria or lysosomes.

In the absence of PDT, cells displayed normal morphology and ACF localized in the cytoplasm and nucleus (Figs. 7(a) and 7(c)). PDT-treated cells cultured under normoxic conditions exhibited shrinkage and blebbing after the treatment (Fig. 7(b)). ACF fluorescence was substantially increased, particularly in the nuclei. Under hypoxic conditions, there were no profound effects of ACF on the intracellular localization and morphology of the cells. PDT-treated cells that were kept under hypoxic conditions displayed a similar degree of shrinkage and blebbing, but a reduced ACF fluorescence intensity (Fig. 7(d)).

3.9 ACF reduces expression of angiogenesis- and survival-associated genes

To investigate whether the increase in PDT efficacy caused by adjuvant ACF was indeed attributable to inhibition of HIF-1, the expression levels of a variety of HIF-1 target genes were determined using qRT-PCR after hypoxic incubation only (CTRL) or after concomitant exposures to ACF, PDT, or the combined ACF + PDT treatment. Genes were clustered according to the relation of their products to angiogenesis, glycolysis, or survival (Fig. 8). A numerical representation of the data is provided in Table 2. PDT strongly induced expression of *PTGS2*, *VEGF*, and *HMOX1* (also shown in Fig. 4(e)). ACF alone and in combination with PDT reduced the extent of *PTGS2* and *VEGF* expression. This observation provides important clues to the mechanisms of enhanced cytotoxicity of ACF + PDT, since the protein products of both genes have been shown to stimulate tumor cell survival post-PDT

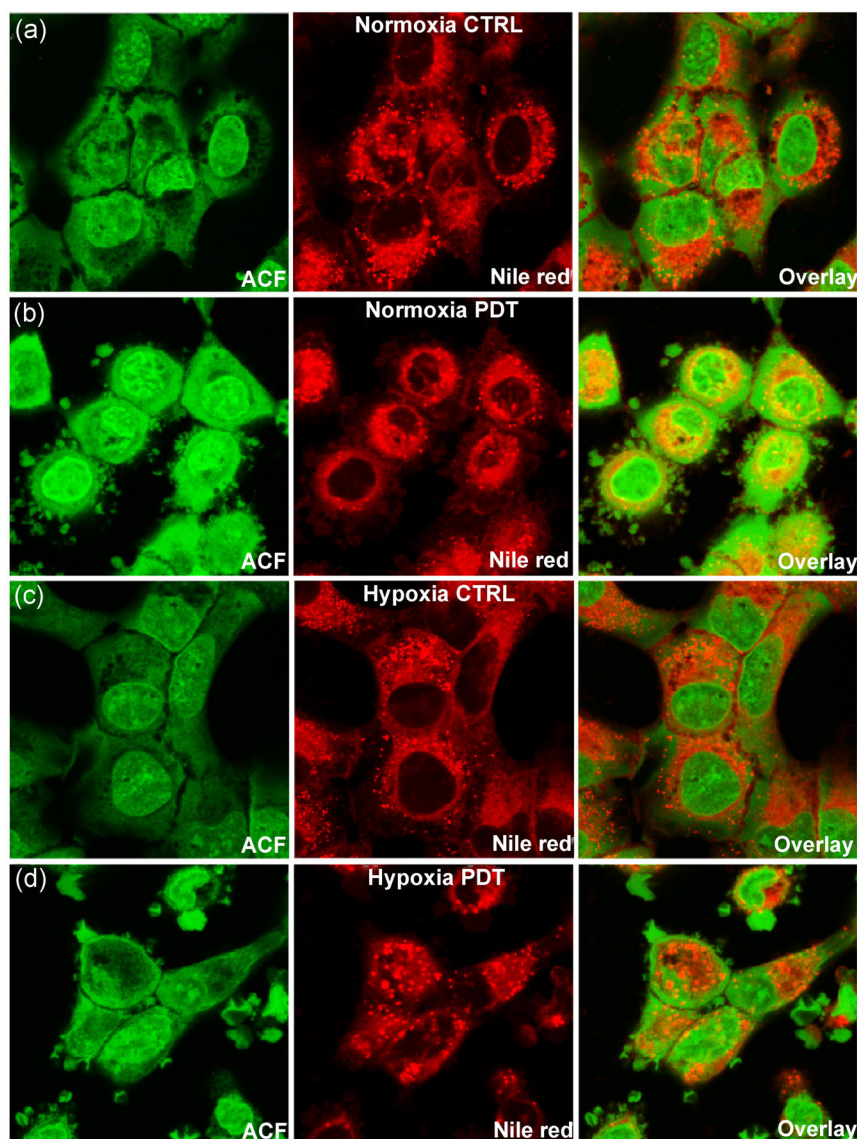


Figure 7 The intracellular localization of ACF was determined in A431 cells using confocal microscopy. Cells were treated as indicated ((a)–(d)) and placed under either normoxic or hypoxic culture conditions in the presence of 3 μ M ACF for 4 h. Cells were fixed and counterstained with the lipophilic dye Nile Red (red), which stains all intracellular membranes. All images were taken with a 63 \times oil immersion lens and digital zoom.

[55, 58–60]. *HMOX1* was also induced by hypoxia and PDT, but its expression was unaltered following ACF pretreatment, suggesting that its expression was modulated by an unknown HIF-1-independent mechanism (e.g., by nuclear factor E2-related factor 2 (NRF2) [61]). *BIRC5*, the gene that encodes survivin—a protein that regulates survival of cancer cells [62]—was found to be downregulated after hypoxia and PDT, but upregulated when the cells were pretreated with ACF. Accordingly, ACF-induced upregulation of survivin may counteract the neoadjuvant efficacy of

this HIF-1 α inhibitor. In the angiogenesis gene cluster, it is interesting to note that *EDN1* mRNA levels were reduced after hypoxia and PDT, yet strongly upregulated following ACF and ACF + PDT treatments. *EDN1* is a putative gene target of activated HIF-1 that induces proliferation by binding to the EDN-1-associated receptor (ETAR), which, in turn, activates β -catenin and induces expression of *CCND1*, the cyclin D1 gene. *EDN1* also stimulates cell survival by promoting nuclear factor κ B activity and subsequent upregulation of *BCL2* and *BIRC5*, as well as by

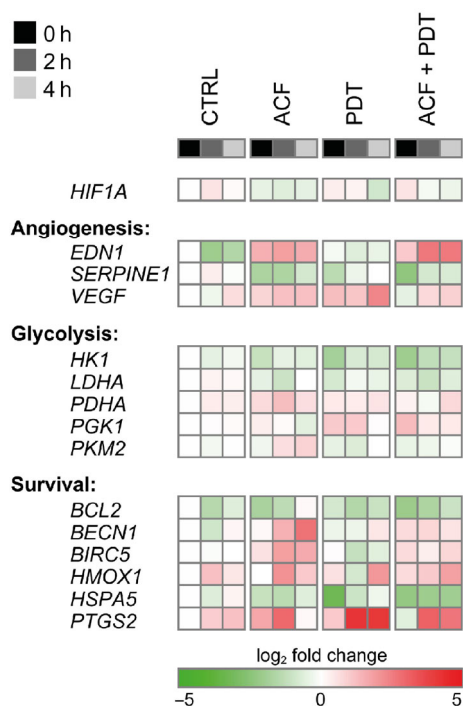


Figure 8 Heat map of gene expression patterns in A431 cells analyzed 0, 2, or 4 h post-treatment under hypoxic conditions. The plotted data represent the \log_2 -transformed fold changes of each data point in relation to control (CTRL) values measured at 0 h in normoxic conditions. Upregulated and downregulated genes are depicted in red and green, respectively.

stimulating COX-2 activity. Consequently, *EDN1* excreted from tumor cells stimulates angiogenesis, proliferation, and survival (for a detailed review about the signaling events downstream of *EDN1*, see Ref. [63]). In contrast with the previous, an increase in *EDN1* expression after ACF treatment, especially following its combined administration with PDT, may indicate that HIF-1 inhibits expression of this gene rather than imparting a stimulating effect. *EDN1* expression may be potentially triggered by PDT via alternative signaling pathways, namely through JUN and FOS transcription factors [63]. Notably, *EDN1* expression was found to be strongly upregulated upon ER stress [64]. PDT-induced *EDN1* upregulation was apparently offset in A431 cells, but ACF-mediated ER stress may have materialized as discussed above.

Most other genes were either slightly up- or downregulated in a treatment-independent fashion. In addition to hypoxia and PDT (Fig. 4(e)), exposure to ACF or to ACF + PDT did not affect expression of glycolysis genes. However, the expression levels of these genes may be influenced by the presence of glucose in the culture medium, which distinguishes this experimental setting from the *in vivo* situation,

Table 2 Mean \pm SD \log_2 -transformed fold-change in mRNA levels of established HIF-1 target genes in control cells or ACF/PDT/ACF + PDT-treated cells as a function of time after PDT

Gene	CTRL			ACF			PDT			ACF + PDT		
	0 h	2 h	4 h	0 h	2 h	4 h	0 h	2 h	4 h	0 h	2 h	4 h
<i>HIF1A</i>	0.00 \pm 0.09	0.58 \pm 0.45	0.12 \pm 0.31	-0.47 \pm 0.42	-1.38 \pm 0.37	-0.48 \pm 0.28	0.41 \pm 0.39	0.28 \pm 0.21	-0.88 \pm 0.27	0.54 \pm 0.43	-0.20 \pm 0.39	-0.42 \pm 0.62
<i>EDN1</i>	0.00 \pm 0.41	-2.00 \pm 0.33	-1.51 \pm 0.13	1.57 \pm 0.28	2.72 \pm 1.28	2.62 \pm 1.19	0.55 \pm 1.25	-0.58 \pm 0.01	-0.38 \pm 0.23	1.10 \pm 0.18	2.65 \pm 0.25	2.63 \pm 0.34
<i>SERPINE 1</i>	0.00 \pm 1.18	0.15 \pm 0.12	0.00 \pm 0.31	-1.65 \pm 0.39	-0.08 \pm 0.93	-0.82 \pm 0.12	-1.33 \pm 0.78	-0.30 \pm 0.15	0.08 \pm 0.36	-2.30 \pm 0.03	-0.83 \pm 0.15	-0.71 \pm 0.23
<i>VEGF</i>	0.00 \pm 0.39	-0.27 \pm 0.54	0.67 \pm 0.38	0.85 \pm 0.18	1.24 \pm 0.56	1.25 \pm 0.40	1.28 \pm 0.50	1.13 \pm 0.31	2.16 \pm 0.55	-0.46 \pm 0.65	0.77 \pm 0.41	0.95 \pm 0.57
<i>HK1</i>	0.00 \pm 1.04	0.27 \pm 0.40	0.00 \pm 0.50	-1.25 \pm 0.64	-0.65 \pm 0.87	0.21 \pm 0.66	-0.34 \pm 0.57	-0.71 \pm 0.48	-0.05 \pm 0.16	-1.06 \pm 0.51	-0.48 \pm 0.19	-0.40 \pm 0.21
<i>LDHA</i>	0.00 \pm 0.38	0.26 \pm 0.68	0.18 \pm 0.06	-0.80 \pm 0.71	-0.18 \pm 0.53	-0.40 \pm 0.40	-0.47 \pm 0.15	-1.03 \pm 0.06	0.02 \pm 0.66	-0.68 \pm 0.34	-1.04 \pm 0.19	0.60 \pm 0.20
<i>PDHA</i>	0.00 \pm 0.42	0.22 \pm 0.80	0.40 \pm 0.46	0.74 \pm 0.47	1.30 \pm 0.81	0.65 \pm 0.08	0.48 \pm 0.22	0.43 \pm 0.18	0.59 \pm 0.31	0.31 \pm 0.18	-0.15 \pm 0.07	0.79 \pm 0.25
<i>PGK1</i>	0.00 \pm 0.36	0.13 \pm 0.53	0.15 \pm 0.65	0.39 \pm 0.21	0.15 \pm 0.43	-0.51 \pm 0.84	1.06 \pm 0.30	1.11 \pm 0.12	0.13 \pm 0.76	1.77 \pm 0.86	1.11 \pm 0.82	0.79 \pm 0.60
<i>PKM2</i>	0.00 \pm 0.29	-0.21 \pm 0.40	0.00 \pm 0.42	-0.24 \pm 0.37	0.66 \pm 0.81	0.91 \pm 0.82	-0.43 \pm 0.44	-0.65 \pm 0.45	0.07 \pm 0.28	0.41 \pm 0.15	-0.27 \pm 0.52	-0.07 \pm 0.35
<i>BCL2</i>	0.00 \pm 0.21	-0.49 \pm 0.21	0.71 \pm 0.14	-0.76 \pm 0.57	-0.34 \pm 0.81	1.14 \pm 0.54	0.48 \pm 0.30	-0.54 \pm 0.47	-0.76 \pm 0.12	-1.14 \pm 0.80	-0.70 \pm 1.15	-0.06 \pm 0.63
<i>BECN1</i>	0.00 \pm 0.50	-0.90 \pm 0.07	0.23 \pm 0.17	1.04 \pm 0.28	1.54 \pm 0.31	2.53 \pm 0.63	0.18 \pm 0.36	-0.30 \pm 0.37	0.55 \pm 0.18	-0.33 \pm 0.40	0.84 \pm 0.29	0.60 \pm 0.23
<i>BIRC5</i>	0.00 \pm 0.42	-0.07 \pm 0.65	0.05 \pm 0.36	0.62 \pm 0.21	1.87 \pm 0.14	1.68 \pm 0.88	0.10 \pm 0.77	-1.12 \pm 0.58	-0.53 \pm 0.22	0.74 \pm 0.18	0.43 \pm 0.55	0.84 \pm 0.49
<i>HMOX1</i>	0.00 \pm 0.19	1.26 \pm 0.48	0.55 \pm 0.16	0.94 \pm 0.41	2.15 \pm 1.35	1.08 \pm 0.68	0.62 \pm 0.90	0.63 \pm 0.11	2.04 \pm 1.10	0.75 \pm 0.41	1.04 \pm 0.28	1.85 \pm 0.04
<i>HSPA5</i>	0.00 \pm 0.81	-0.64 \pm 0.49	0.27 \pm 0.12	-2.23 \pm 0.61	-1.33 \pm 0.78	-1.34 \pm 0.44	-1.11 \pm 1.04	-0.98 \pm 0.22	0.10 \pm 0.13	-3.25 \pm 0.12	-2.05 \pm 0.52	-1.98 \pm 0.24
<i>PTGS2</i>	0.00 \pm 0.48	0.99 \pm 0.33	1.21 \pm 0.10	1.74 \pm 0.11	2.98 \pm 0.82	-1.07 \pm 0.20	1.10 \pm 0.50	4.24 \pm 0.97	4.10 \pm 0.53	-0.53 \pm 0.62	3.14 \pm 0.40	2.72 \pm 0.24

where vascular shutdown is expected to induce a state of tumor hyponutrition [65]. Nonetheless, the glycolysis gene expression data corroborate the lactate excretion results and support the notion that the facilitation of a metabolic switch to anaerobic glycolysis does not underlie the cytoprotective effect of HIF-1 activation *in vitro*.

In summary, our data on the effects of PDT and combined action of PDT and hypoxia corroborate the pro-survival role of HIF-1 after PDT. PDT led to transcriptional upregulation of *VEGF*, *PTGS2*, and *HMOX1* genes, whose protein products, VEGF, COX-2, and HO-1, have been implicated in the regulation of tumor cell survival after PDT [22, 23, 59–61, 66–73]. Accordingly, HIF-1 inhibition by ACF exerted an adjuvant effect on PDT and subsequent hypoxia and

reduced expression of *VEGF* and *PTGS2*, accentuating a pharmacological value of this HIF-1 inhibitor for PDT.

3.10 ACF, PDT, and hypoxia do not induce DNA damage

Many anticancer agents exert chemotherapeutic effects by inducing DNA damage, which signals the p53 tumor suppressor protein to induce cell cycle arrest and apoptosis [74, 75]. Since p53 can affect HIF-1 activation [76] and ACF was prominently present in the nucleus (Fig. 7), we investigated whether ACF induced DNA damage under any of the experimental conditions. Cells were stained for the presence of DNA double-strand breaks using the epigenetic marker phospho-H2AX [77]. The results suggest that there was preexisting DNA damage in A431 cells (Fig. 9(a)),

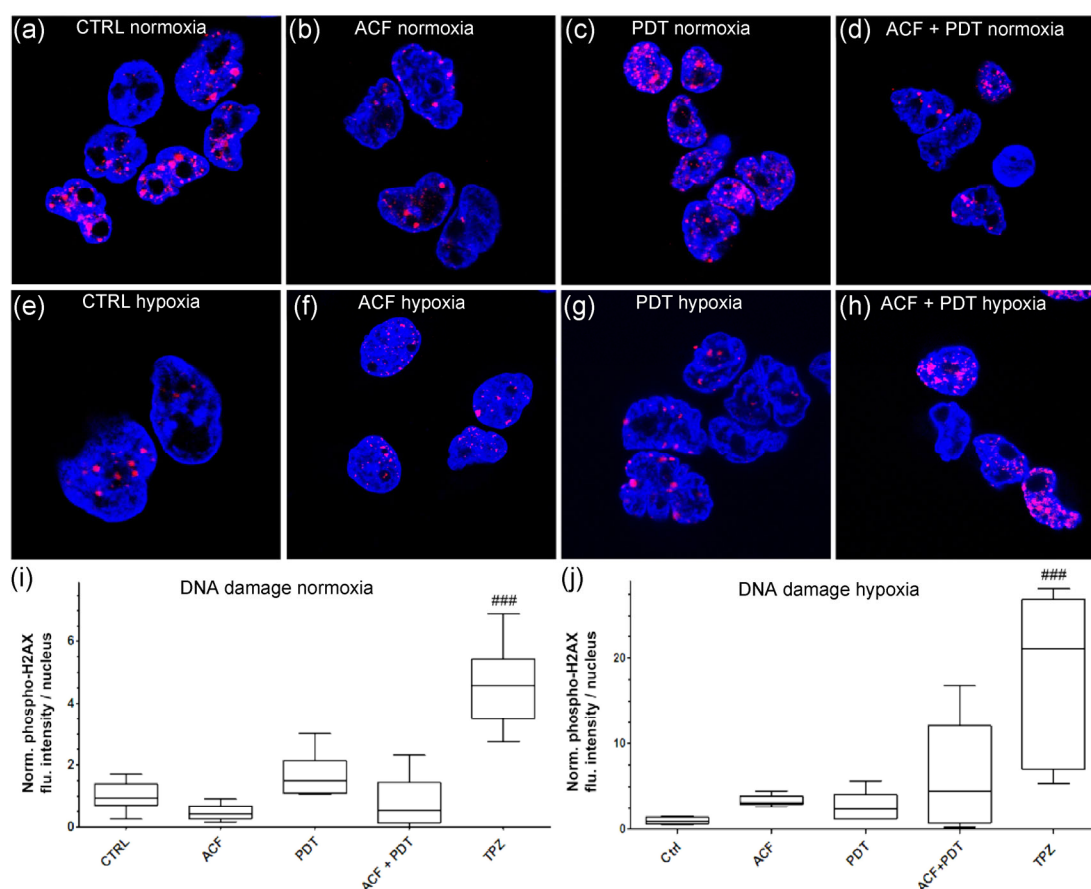


Figure 9 (a)–(h) Analysis of DNA damage in A431 cells after CTRL treatment ((a) and (e)) and treatments with ACF ((b) and (f)), PDT ((c) and (g)), and ACF + PDT ((d) and (h)). Cells were kept for 4 h under normoxic ((a)–(d)) or hypoxic conditions ((e)–(h)) post-treatment. Cells were stained with DAPI (nuclei, blue) and phospho-H2AX (DNA double-strand breaks, red). (i) and (j) Box-whisker plots of the mean phospho-H2AX fluorescence intensity per cell within each treatment group. (i) represents cells kept under normoxic conditions after PDT, (j) represents cells that were kept under hypoxic conditions after PDT. Cells treated for 24 h with TPZ were included as positive control. Data represent the mean values of 6 observations.

which was not exacerbated by any of the experimental conditions (Figs. 9(b)–9(d)), regardless of oxygen tension (Figs. 9(e)–9(h)). Preexisting DNA damage confirms the fact that A431 cells largely lack the functional p53 protein [78, 79], an assumption also corroborated by the absence of fragmented nuclei. Quantitative analysis of the degree of DNA damage is presented in Figs. 9(i) and 9(j). As a positive control for DNA damage, cells were incubated for 24 h with TPZ, a DNA-damaging agent that becomes more active under hypoxic conditions [80]. In conclusion, ACF does not induce DNA damage despite its nuclear localization.

3.11 Co-encapsulation of ACF into ZnPC-ETLs leads to augmented cell death after PDT

In a final set of experiments, we determined whether liposomal co-encapsulation of both ACF and ZnPC into a single formulation was feasible and whether such preparation could enhance PDT efficacy in comparison to the effect of liposomes without ACF. ACF-ZnPC-ETLs were prepared at increasing ACF:lipid concentrations

and a constant ZnPC:lipid concentration, as shown in Fig. 10(a). ACF-ZnPC-ETLs entrapped 3.31% of ACF on average, resulting in encapsulation efficiencies of 0.46%, 6.02%, and 3.45% for formulations 2 (ACF:lipid ratio 0.001), 3 (ACF:lipid ratio 0.01), and 4 (ACF:lipid ratio 0.1), respectively. The ZnPC encapsulation efficiency was 100% for all formulations, which is in agreement with Broekgaarden et al. [7], and indicates that ZnPC is not extracted from the liposomes during the liposomal preparation procedure (which includes size exclusion chromatography). The liposomes were stable in terms of size and PDI during a period of 14 days.

Following 12-h exposure of cells to ACF-ETLs (total lipid concentration of 500 μM), only formulation 4 displayed mild toxicity (Fig. 10(b)), which was in agreement with the results in Fig. 6(c) ($\sim 5 \mu\text{M}$ of free ACF was mildly toxic to cells). As expected, intracellular ACF levels reached a maximum when cells were incubated with formulation 4 (Fig. 10(c), green line). When liposomes containing both ZnPC and

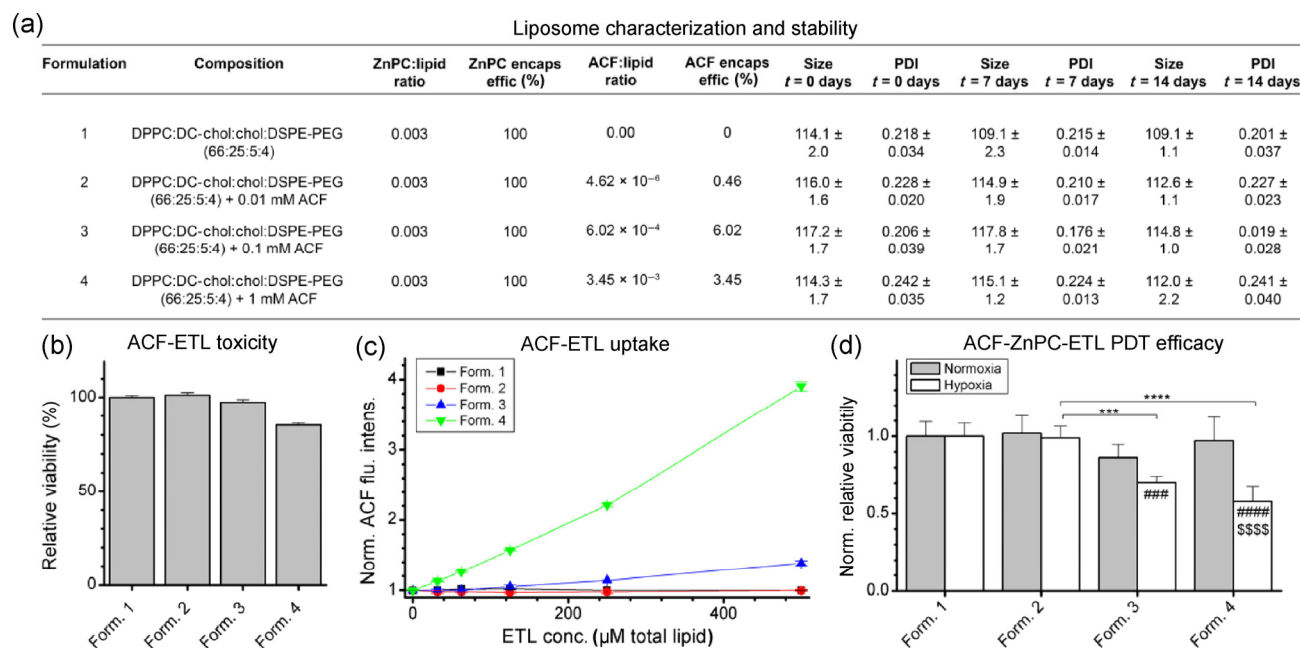


Figure 10 (a) Physical properties and stability of ACF-ZnPC-ETLs. (b) Dark toxicity of 500 μM ACF-ETLs in A431 cells following 12-h incubation under standard culture conditions. Data represent the mean \pm SD of 2 observations. (c) Normalized intracellular ACF fluorescence intensity values following 12-h incubation with ACF-ETLs. ACF fluorescence was corrected for the protein content (SRB method). Data represent the mean \pm SD of 2 observations. (d) PDT efficacy of ZnPC-ACF-ETLs was determined in A431 cells that were incubated for 24 h with liposomes and subsequently treated with PDT. After 24 h of post-PDT incubation under normoxic (gray bars) or hypoxic culture conditions (white bars), viability was determined with the SRB method. Data were normalized to the parameters of viability of formulation 1, which did not contain ACF. Data represent the mean \pm SD of 6 observations.

ACF were used for PDT and cells were incubated under normoxic conditions, there was no significant adjuvant effect of ACF on the PDT efficacy (Fig. 10(d), gray bars). When cells were incubated under hypoxic conditions after PDT, however, a synergistic effect of ACF was observed with respect to PDT efficacy (Fig. 10(d), white bars). It should be noted that these effects were only visible at 24 h post-PDT following 24-h incubation with ACF. The adjuvant effect of ACF was not observed when shorter intervals between PDT and cell death analysis (4 h) were used or when incubation times were shorter (1 h) (data not shown). These results corroborated the findings illustrated in Fig. 6(d), that the most potent adjuvant effect of ACF was observed when cells were incubated under hypoxic conditions following PDT. Taken together, these results demonstrated that co-encapsulation of ACF into ZnPC-ETLs for drug delivery is technically feasible and that this preparation can enhance tumor cell killing efficacy of PDT by inhibiting the propensity of cells to adapt to hypoxic circumstances.

4 Conclusion

Given that activation of HIF-1 by PDT has been well documented and since overexpression of HIF-1 has been associated with decreased susceptibility of tumors and tumor cells to PDT, this study aimed to determine the *in vitro* effect of a combined exposure to PDT and ACF, a drug that inhibits HIF-1. The results of this study are clearly in favor of such a combination therapy since inhibition of HIF-1 with ACF in cultured A431 cells significantly increased PDT efficacy. Moreover, co-encapsulation of ACF and ZnPC into a single liposomal formulation was practically feasible and this preparation also augmented PDT efficacy. Further *in vivo* investigations on the (neo)adjuvant potential of ACF during PDT are warranted to extrapolate these findings in the context of vascular shutdown, hypoxia, hyponutrition, as well as changes in angiogenic signaling and the tumor microenvironment. Since HIF-1 is constitutively active in most—if not all—tumors and has been associated with therapy resistance, this study further underscores the potential of ACF in cancer therapy.

Acknowledgements

This work was supported by grants from the Dutch Anti-Cancer Foundation (Stichting Nationaal Fonds Tegen Kanker) in Amsterdam and the Phospholipid Research Center in Heidelberg (MH). The authors are grateful to Gerben Koning for provision of the A431 cells, Marcel Dirkes and Adrie Maas for input regarding the hypoxic incubator, and Ron Hoebe, Daisy Picavet, and Berend Hooibrink for the technical assistance with confocal microscopy and flow cytometry.

References

- [1] Plaetzer, K.; Krammer, B.; Berlanda, J.; Berr, F.; Kiesslich, T. Photophysics and photochemistry of photodynamic therapy: Fundamental aspects. *Lasers Med. Sci.* **2009**, *24*, 259–268.
- [2] Castano, A. P.; Mroz, P.; Hamblin, M. R. Photodynamic therapy and anti-tumour immunity. *Nat. Rev. Cancer* **2006**, *6*, 535–545.
- [3] Pinthus, J. H.; Bogaards, A.; Weersink, R.; Wilson, B. C.; Trachtenberg, J. Photodynamic therapy for urological malignancies: Past to current approaches. *J. Urol.* **2006**, *175*, 1201–1207.
- [4] Wildeman, M. A. M.; Nyst, H. J.; Karakullukcu, B.; Tan, B. I. Photodynamic therapy in the therapy for recurrent/persistent nasopharyngeal cancer. *Head Neck Oncol.* **2009**, *1*, 40.
- [5] O'Connor, A. E.; Gallagher, W. M.; Byrne, A. T. Porphyrin and nonporphyrin photosensitizers in oncology: Preclinical and clinical advances in photodynamic therapy. *Photochem. Photobiol.* **2009**, *85*, 1053–1074.
- [6] Weijer, R.; Broekgaarden, M.; Kos, M.; Vught, R.; Rauws, E. A. J.; van Gulik, T. M.; Storm, G.; Heger, M. Enhancing photodynamic therapy of refractory solid cancers: Combining second-generation photosensitizers with multi-targeted liposomal delivery. *J. Photochem. Photobiol. C: Photochem. Rev.* **2015**, *23*, 103–131.
- [7] Broekgaarden, M.; de Kroon, A. I. P. M.; van Gulik, T. M.; Heger, M. Development and *in vitro* proof-of-concept of interstitially targeted zinc-phthalocyanine liposomes for photodynamic therapy. *Curr. Med. Chem.* **2014**, *21*, 377–391.
- [8] Aguilar, G.; Choi, B.; Broekgaarden, M.; Yang, O.; Yang, B.; Ghasri, P.; Chen, J. K.; Bezemer, R.; Nelson, J.; van Drooge, A. et al. An overview of three promising mechanical, optical, and biochemical engineering approaches to improve selective photothermolysis of refractory port wine stains. *Ann. Biomed. Eng.* **2012**, *40*, 486–506.

- [9] Deshpande, P. P.; Biswas, S.; Torchilin, V. P. Current trends in the use of liposomes for tumor targeting. *Nanomedicine* **2013**, *8*, DOI: 10.2217/nnm.13.118.
- [10] Maeda, H. The enhanced permeability and retention (EPR) effect in tumor vasculature: The key role of tumor-selective macromolecular drug targeting. *Adv. Enzyme Regul.* **2001**, *41*, 189–207.
- [11] Abu Lila, A. S.; Ishida, T.; Kiwada, H. Targeting anticancer drugs to tumor vasculature using cationic liposomes. *Pharm. Res.* **2010**, *27*, 1171–1183.
- [12] Campbell, R. B.; Ying, B.; Kuesters, G. M.; Hemphill, R. Fighting cancer: From the bench to bedside using second generation cationic liposomal therapeutics. *J. Pharm. Sci.* **2009**, *98*, 411–429.
- [13] Thurston, G.; McLean, J. W.; Rizen, M.; Baluk, P.; Haskell, A.; Murphy, T. J.; Hanahan, D.; McDonald, D. M. Cationic liposomes target angiogenic endothelial cells in tumors and chronic inflammation in mice. *J. Clin. Invest.* **1998**, *101*, 1401–1413.
- [14] Broekgaarden, M.; Weijer, R.; van Gulik, T. M.; Hamblin, M. R.; Heger, M. Tumor cell survival pathways activated by photodynamic therapy: A molecular basis for pharmacological inhibition strategies. *Cancer Metast. Rev.* **2015**, *34*, 643–690.
- [15] Denko, N. C. Hypoxia, HIF1 and glucose metabolism in the solid tumour. *Nat. Rev. Cancer* **2008**, *8*, 705–713.
- [16] Bracken, C. P.; Whitelaw, M. L.; Peet, D. J. The hypoxia-inducible factors: Key transcriptional regulators of hypoxic responses. *Cell. Mol. Life Sci.* **2003**, *60*, 1376–1393.
- [17] Rohwer, N.; Cramer, T. Hypoxia-mediated drug resistance: Novel insights on the functional interaction of HIFs and cell death pathways. *Drug. Resist. Updat.* **2011**, *14*, 191–201.
- [18] Meijer, T. W. H.; Kaanders, J. H. A. M.; Span, P. N.; Bussink, J. Targeting hypoxia, HIF-1, and tumor glucose metabolism to improve radiotherapy efficacy. *Clin. Cancer Res.* **2012**, *18*, 5585–5594.
- [19] Mitra, S.; Cassar, S. E.; Niles, D. J.; Puskas, J. A.; Frelinger, J. G.; Foster, T. H. Photodynamic therapy mediates the oxygen-independent activation of hypoxia-inducible factor 1 α . *Mol. Cancer Ther.* **2006**, *5*, 3268–3274.
- [20] Krieg, R. C.; Raupach, K.; Ren, Q.; Schwamborn, K.; Knuechel, R. Analyzing effects of photodynamic therapy with 5-aminolevulinic acid (ALA) induced protoporphyrin IX (PPIX) in urothelial cells using reverse phase protein arrays. *Photochem. Photobiol. Sci.* **2007**, *6*, 1296–1305.
- [21] Ferrario, A.; Gomer, C. J. Targeting the 90 kDa heat shock protein improves photodynamic therapy. *Cancer Lett.* **2010**, *289*, 188–194.
- [22] Ferrario, A.; Gomer, C. Avastin enhances photodynamic therapy treatment of Kaposi's sarcoma in a mouse tumor model. *J. Environ. Pathol. Toxicol. Oncol.* **2006**, *25*, 251–260.
- [23] Ferrario, A.; von Tiehl, K.; Wong, S.; Luna, M.; Gomer, C. J. Cyclooxygenase-2 inhibitor treatment enhances photodynamic therapy-mediated tumor response. *Cancer Res.* **2002**, *62*, 3956–3961.
- [24] Ji, Z. Y.; Yang, G. R.; Shahzidi, S.; Tkacz-Stachowska, K.; Suo, Z. H.; Nesland, J. M.; Peng, Q. Induction of hypoxia-inducible factor-1 α overexpression by cobalt chloride enhances cellular resistance to photodynamic therapy. *Cancer Lett.* **2006**, *244*, 182–189.
- [25] Koukourakis, M. I.; Giatromanolaki, A.; Skarlatos, J.; Corti, L.; Blandamura, S.; Piazza, M.; Gatter, K. C.; Harris, A. L. Hypoxia inducible factor (HIF-1 α and HIF-2 α) expression in early esophageal cancer and response to photodynamic therapy and radiotherapy. *Cancer Res.* **2001**, *61*, 1830–1832.
- [26] Semenza, G. L. Hypoxia-inducible factors: Mediators of cancer progression and targets for cancer therapy. *Trends Pharmacol. Sci.* **2012**, *33*, 207–214.
- [27] Ratcliffe, P. J. Oxygen sensing and hypoxia signalling pathways in animals: The implications of physiology for cancer. *J. Physiol.* **2013**, *591*, 2027–2042.
- [28] Salceda, S.; Caro, J. Hypoxia-inducible factor 1 α (HIF-1 α) protein is rapidly degraded by the ubiquitin-proteasome system under normoxic conditions. *J. Biol. Chem.* **1997**, *272*, 22642–22647.
- [29] Maxwell, P. H.; Wiesener, M. S.; Chang, G.-W.; Clifford, S. C.; Vaux, E. C.; Cockman, M. E.; Wykoff, C. C.; Pugh, C. W.; Maher, E. R.; Ratcliffe, P. J. The tumour suppressor protein VHL targets hypoxia-inducible factors for oxygen-dependent proteolysis. *Nature* **1999**, *399*, 271–275.
- [30] Chilov, D.; Camenisch, G.; Kvietikova, I.; Ziegler, U.; Gassmann, M.; Wenger, R. H. Induction and nuclear translocation of hypoxia-inducible factor-1 (HIF-1): Heterodimerization with ARNT is not necessary for nuclear accumulation of HIF-1 α . *J. Cell Sci.* **1999**, *112*, 1203–1212.
- [31] Lu, H. S.; Dalgard, C. L.; Mohyeldin, A.; McFate, T.; Tait, A. S.; Verma, A. Reversible inactivation of HIF-1 prolyl hydroxylases allows cell metabolism to control basal HIF-1. *J. Biol. Chem.* **2005**, *280*, 41928–41939.
- [32] Schofield, C. J.; Ratcliffe, P. J. Oxygen sensing by HIF hydroxylases. *Nat. Rev. Mol. Cell Biol.* **2004**, *5*, 343–354.
- [33] Schödel, J.; Oikonomopoulos, S.; Ragoussis, J.; Pugh, C. W.; Ratcliffe, P. J.; Mole, D. R. High-resolution genome-wide mapping of HIF-binding sites by ChIP-seq. *Blood* **2011**, *117*, e207–e217.
- [34] Semenza, G. L. Targeting HIF-1 for cancer therapy. *Nat. Rev. Cancer* **2003**, *3*, 721–732.
- [35] Bellot, G.; Garcia-Medina, R.; Gounon, P.; Chiche, J.; Roux, D.; Pouyssegur, J.; Mazure, N. M. Hypoxia-induced autophagy is mediated through hypoxia-inducible factor induction of

- BNIP3 and BNIP3L via their BH3 domains. *Mol. Cell. Biol.* **2009**, *29*, 2570–2581.
- [36] Lee, K.; Zhang, H. F.; Qian, D. Z.; Rey, S.; Liu, J. O.; Semenza, G. L. Acriflavine inhibits HIF-1 dimerization, tumor growth, and vascularization. *Proc. Natl. Acad. Sci. USA* **2009**, *106*, 17910–17915.
- [37] Rouser, G.; Fleischer, S.; Yamamoto, A. Two dimensional thin layer chromatographic separation of polar lipids and determination of phospholipids by phosphorus analysis of spots. *Lipids* **1970**, *5*, 494–496.
- [38] Lasch, J.; Weissig, V.; Brandl, M. Preparation of liposomes. In *Liposomes*, 2nd ed.; Torchilin, V. P.; Weissig, V., Eds.; Oxford University Press: New York, 2003; pp 3–29.
- [39] Kloek, J. J.; Maréchal, X.; Roelofsen, J.; Houtkooper, R. H.; van Kuilenburg, A. B.; Kulik, W.; Bezemer, R.; Nevière, R.; van Gulik, T. M.; Heger, M. Cholestasis is associated with hepatic microvascular dysfunction and aberrant energy metabolism before and during ischemia-reperfusion. *Antioxid. Redox Signal.* **2012**, *17*, 1109–1123.
- [40] Vichai, V.; Kirtikara, K. Sulforhodamine B colorimetric assay for cytotoxicity screening. *Nat. Protoc.* **2006**, *1*, 1112–1116.
- [41] Ramakers, C.; Ruijter, J. M.; Deprez, R. H. L.; Moorman, A. F. M. Assumption-free analysis of quantitative real-time polymerase chain reaction (PCR) data. *Neurosci. Lett.* **2003**, *339*, 62–66.
- [42] Trott, O.; Olson, A. J. Autodock Vina: Improving the speed and accuracy of docking with a new scoring function, efficient optimization, and multithreading. *J. Comput. Chem.* **2010**, *31*, 455–461.
- [43] Mayo, S. L.; Olafson, B. D.; Goddard, W. A. Dreiding: A generic force field for molecular simulations. *J. Phys. Chem.* **1990**, *94*, 8897–8909.
- [44] Gasteiger, J.; Marsili, M. Iterative partial equalization of orbital electronegativity—A rapid access to atomic charges. *Tetrahedron* **1980**, *36*, 3219–3228.
- [45] Barbosa, L. R. S.; Ortore, M. G.; Spinozzi, F.; Mariani, P.; Bernstorff, S.; Itri, R. The importance of protein–protein interactions on the pH-induced conformational changes of bovine serum albumin: A small-angle X-ray scattering study. *Biophys. J.* **2010**, *98*, 147–157.
- [46] Loboda, A.; Jazwa, A.; Wegiel, B.; Jozkowicz, A.; Dulak, J. Heme oxygenase-1-dependent and -independent regulation of angiogenic genes expression: Effect of cobalt protoporphyrin and cobalt chloride on VEGF and IL-8 synthesis in human microvascular endothelial cells. *Cell. Mol. Biol. (Noisy-le-grand)* **2005**, *51*, 347–355.
- [47] Nowis, D.; Legat, M.; Grzela, T.; Niderla, J.; Wilczek, E.; Wilczynski, G. M.; Głodkowska, E.; Mrówka, P.; Issat, T.; Dulak, J. et al. Heme oxygenase-1 protects tumor cells against photodynamic therapy-mediated cytotoxicity. *Oncogene* **2006**, *25*, 3365–3374.
- [48] Berra, E.; Roux, D.; Richard, D. E.; Pouyssegur, J. Hypoxia-inducible factor-1 α (HIF-1 α) escapes O₂-driven proteasomal degradation irrespective of its subcellular localization: Nucleus or cytoplasm. *EMBO Rep.* **2001**, *2*, 615–620.
- [49] Newby, D.; Marks, L.; Lyall, F. Dissolved oxygen concentration in culture medium: Assumptions and pitfalls. *Placenta* **2005**, *26*, 353–357.
- [50] Fears, C. Y.; Gladson, C. L.; Woods, A. Syndecan-2 is expressed in the microvasculature of gliomas and regulates angiogenic processes in microvascular endothelial cells. *J. Biol. Chem.* **2006**, *281*, 14533–14536.
- [51] Ran, S.; Downes, A.; Thorpe, P. E. Increased exposure of anionic phospholipids on the surface of tumor blood vessels. *Cancer Res.* **2002**, *62*, 6132–6140.
- [52] Kaidi, A.; Qualtrough, D.; Williams, A. C.; Paraskeva, C. Direct transcriptional up-regulation of cyclooxygenase-2 by hypoxia-inducible factor (HIF)-1 promotes colorectal tumor cell survival and enhances HIF-1 transcriptional activity during hypoxia. *Cancer Res.* **2006**, *66*, 6683–6691.
- [53] Hu, J.; Discher, D. J.; Bishopric, N. H.; Webster, K. A. Hypoxia regulates expression of the endothelin-1 gene through a proximal hypoxia-inducible factor-1 binding site on the antisense strand. *Biochem. Biophys. Res. Commun.* **1998**, *245*, 894–899.
- [54] Fink, T.; Kazlauskas, A.; Poellinger, L.; Ebbesen, P.; Zachar, V. Identification of a tightly regulated hypoxia-response element in the promoter of human plasminogen activator inhibitor-1. *Blood* **2002**, *99*, 2077–2083.
- [55] Zhou, Q. Y.; Olivo, M.; Lye, K. Y. K.; Moore, S.; Sharma, A.; Chowbay, B. Enhancing the therapeutic responsiveness of photodynamic therapy with the antiangiogenic agents SU5416 and SU6668 in murine nasopharyngeal carcinoma models. *Cancer Chemother. Pharmacol.* **2005**, *56*, 569–577.
- [56] Key, J.; Scheuermann, T. H.; Anderson, P. C.; Daggett, V.; Gardner, K. H. Principles of ligand binding within a completely buried cavity in HIF2 α PAS-B. *J. Am. Chem. Soc.* **2009**, *131*, 17647–17654.
- [57] Tennant, D. A.; Frezza, C.; MacKenzie, E. D.; Nguyen, Q. D.; Zheng, L.; Selak, M. A.; Roberts, D. L.; Dive, C.; Watson, D. G.; Aboagye, E. O. et al. Reactivating HIF prolyl hydroxylases under hypoxia results in metabolic catastrophe and cell death. *Oncogene* **2009**, *28*, 4009–4021.
- [58] Solban, N.; Selbo, K.; Sinha, A. K.; Chang, S. K.; Hasan, T. Mechanistic investigation and implications of photodynamic therapy induction of vascular endothelial growth factor in prostate cancer. *Cancer Res.* **2006**, *66*, 5633–5640.
- [59] Makowski, M.; Grzela, T.; Niderla, J.; Łazarczyk, M.; Mróz, P.; Kopeć, M.; Legat, M.; Strusińska, K.; Koziak, K.; Nowis, D. et al. Inhibition of cyclooxygenase-2 indirectly

- potentiates antitumor effects of photodynamic therapy in mice. *Clin. Cancer Res.* **2003**, *9*, 5417–5422.
- [60] Hendrickx, N.; Volanti, C.; Moens, U.; Seternes, O. M.; de Witte, P.; Vandenheede, J. R.; Piette, J.; Agostinis, P. Up-regulation of cyclooxygenase-2 and apoptosis resistance by p38 MAPK in hypericin-mediated photodynamic therapy of human cancer cells. *J. Biol. Chem.* **2003**, *278*, 52231–52239.
- [61] Kocanova, S.; Buytaert, E.; Matroule, J.-Y.; Piette, J.; Golab, J.; de Witte, P.; Agostinis, P. Induction of heme-oxygenase 1 requires the p38^{MAPK} and PI3K pathways and suppresses apoptotic cell death following hypericin-mediated photodynamic therapy. *Apoptosis* **2007**, *12*, 731–741.
- [62] Lladser, A.; Sanhueza, C.; Kiessling, R.; Quest, A. F. G. Is survivin the potential Achilles' heel of cancer? *Adv. Cancer Res.* **2011**, *111*, 1–37.
- [63] Rosanò, L.; Spinella, F.; Bagnato, A. Endothelin 1 in cancer: Biological implications and therapeutic opportunities. *Nat. Rev. Cancer* **2013**, *13*, 637–651.
- [64] Padilla, J.; Jenkins, N. T. Induction of endoplasmic reticulum stress impairs insulin-stimulated vasomotor relaxation in rat aortic rings: Role of endothelin-1. *J. Physiol. Pharmacol.* **2013**, *64*, 557–564.
- [65] Dolmans, D. E. J. G. J.; Kadambi, A.; Hill, J. S.; Waters, C. A.; Robinson, B. C.; Walker, J. P.; Fukumura, D.; Jain, R. K. Vascular accumulation of a novel photosensitizer, MV6401, causes selective thrombosis in tumor vessels after photodynamic therapy. *Cancer Res.* **2002**, *62*, 2151–2156.
- [66] Nowis, D.; Bugajski, M.; Winiarska, M.; Bil, J.; Szokalska, A.; Salwa, P.; Issat, T.; Was, H.; Jozkowicz, A.; Dulak, J. et al. Zinc protoporphyrin IX, a heme oxygenase-1 inhibitor, demonstrates potent antitumor effects but is unable to potentiate antitumor effects of chemotherapeutics in mice. *BMC Cancer* **2008**, *8*, 197.
- [67] Harvey, E. H.; Webber, J.; Kessel, D.; Fromm, D. Killing tumor cells: The effect of photodynamic therapy using mono-l-aspartyl chlorine and NS-398. *Am. J. Surg.* **2005**, *189*, 302–305.
- [68] Ferrario, A.; Lim, S.; Xu, F.; Luna, M.; Gaffney, K. J.; Petasis, N. A.; Schönthal, A. H.; Gomer, C. J. Enhancement of photodynamic therapy by 2,5-dimethyl celecoxib, a non-cyclooxygenase-2 inhibitor analog of celecoxib. *Cancer Lett.* **2011**, *304*, 33–40.
- [69] Grimm, S.; Mvondo, D.; Grune, T.; Breusing, N. The outcome of 5-ALA-mediated photodynamic treatment in melanoma cells is influenced by vitamin C and heme oxygenase-1. *Biofactors* **2011**, *37*, 17–24.
- [70] Frank, J.; Lornejad-Schäfer, M. R.; Schöffl, H.; Flaccus, A.; Lambert, C.; Biesalski, H. K. Inhibition of heme oxygenase-1 increases responsiveness of melanoma cells to ALA-based photodynamic therapy. *Int. J. Oncol.* **2007**, *31*, 1539–1545.
- [71] Miyake, M.; Ishii, M.; Kawashima, K.; Kodama, T.; Sugano, K.; Fujimoto, K.; Hirao, Y. siRNA-mediated knockdown of the heme synthesis and degradation pathways: Modulation of treatment effect of 5-aminolevulinic acid-based photodynamic therapy in urothelial cancer cell lines. *Photochem. Photobiol.* **2009**, *85*, 1020–1027.
- [72] Akita, Y.; Kozaki, K.; Nakagawa, A.; Saito, T.; Ito, S.; Tamada, Y.; Fujiwara, S.; Nishikawa, N.; Uchida, K.; Yoshikawa, K. et al. Cyclooxygenase-2 is a possible target of treatment approach in conjunction with photodynamic therapy for various disorders in skin and oral cavity. *Br. J. Dermatol.* **2004**, *151*, 472–480.
- [73] Ferrario, A.; Fisher, A. M.; Rucker, N.; Gomer, C. J. Celecoxib and NS-398 enhance photodynamic therapy by increasing *in vitro* apoptosis and decreasing *in vivo* inflammatory and angiogenic factors. *Cancer Res.* **2005**, *65*, 9473–9478.
- [74] Levine, A. J. p53, the cellular gatekeeper for growth and division. *Cell* **1997**, *88*, 323–331.
- [75] Villunger, A.; Michalak, E. M.; Coutas, L.; Müllauer, F.; Böck, G.; Ausserlechner, M. J.; Adams, J. M.; Strasser, A. p53- and drug-induced apoptotic responses mediated by BH3-only proteins Puma and Noxa. *Science* **2003**, *302*, 1036–1038.
- [76] Ravi, R.; Mookerjee, B.; Bhujwalla, Z. M.; Sutter, C. H.; Artemov, D.; Zeng, Q. W.; Dillehay, L. E.; Madan, A.; Semenza, G. L.; Bedi, A. Regulation of tumor angiogenesis by p53-induced degradation of hypoxia-inducible factor 1 α . *Genes Dev.* **2000**, *14*, 34–44.
- [77] Rogakou, E. P.; Pilch, D. R.; Orr, A. H.; Ivanova, V. S.; Bonner, W. M. DNA double-stranded breaks induce histone H2AX phosphorylation on serine 139. *J. Biol. Chem.* **1998**, *273*, 5858–5868.
- [78] Reiss, M.; Brash, D. E.; Muñoz-Antonia, T.; Simon, J. A.; Ziegler, A.; Vellucci, V. F.; Zhou, Z. L. Status of the p53 tumor suppressor gene in human squamous carcinoma cell lines. *Oncol. Res.* **1992**, *4*, 349–357.
- [79] Kwok, T. T.; Mok, C. H.; Menton-Brennan, L. Up-regulation of a mutant form of p53 by doxorubicin in human squamous carcinoma cells. *Cancer Res.* **1994**, *54*, 2834–2836.
- [80] Daniels, J. S.; Gates, K. S.; Tronche, C.; Greenberg, M. M. Direct evidence for bimodal DNA damage induced by tirapazamine. *Chem. Res. Toxicol.* **1998**, *11*, 1254–1257.
- [81] Gheonea, D. I.; Cârțână, T.; Ciurea, T.; Popescu, C.; Bădărău, A.; Săftoiu, A. Confocal laser endomicroscopy and immunoendoscopy for real-time assessment of vascularization in gastrointestinal malignancies. *World J. Gastroenterol.* **2011**, *17*, 21–27.